A Joint Global Carbon Inversion System Using Both CO_2 and CO_2 Atmospheric Concentration Data

Jing M. Chen[1,2], Gang Mo[2], Feng Deng[2]

[1]International Institute of Earth System Science

Nanjing University

22 Hankou Road, Nanjing, Jiangsu

China, 210093

and

[2]Department of Geography and Program in Planning

University of Toronto

100 St. George Street

Toronto, Ontario, Canada M5S 3G3

(Revision submitted to *Geoscientific Model Development*)

November 2016

Corresponding author: Jing M. Chen, chenj@geog.utoronto.ca

20   **Abstract**

21   Observations of $^{13}CO_2$ at 73 sites compiled in the GLOBALVIEW database are used for an

22   additional constraint in a global atmospheric inversion of the surface CO_2 flux using CO_2

23   observations at 210 sites (62 collocated with $^{13}CO_2$ sites) for the 2002-2004 period for 39 land

24   regions and 11 ocean regions. This constraint is implemented using prior CO_2 fluxes estimated with a

25   terrestrial ecosystem model and an ocean model. These models simulate $^{13}CO_2$ discrimination rates

26   of terrestrial photosynthesis and ocean-atmosphere diffusion processes. In both models, the $^{13}CO_2$

27   disequilibrium between fluxes to and from the atmosphere is considered due to the historical change

28   in atmospheric $^{13}CO_2$ concentration. This joint inversion system using both $^{13}CO_2$ and CO_2

29   observations is effectively a double deconvolution system with consideration of the spatial variations

30   of isotopic discrimination and disequilibrium. Compared to the CO_2-only inversion, this $^{13}CO_2$

31   constraint on the inversion considerably reduces the total land carbon sink from 3.40±0.84 to

32   2.53±0.93 Pg C y^{-1} but increases the total oceanic carbon sink from 1.48±0.40 to 2.36 ±0.49 Pg C y^{-1}.

33   This constraint also changes the spatial distribution of the carbon sink. The largest sink increase

34   occurs in Amazon, while the largest source increases are in southern Africa, and Asia, where CO_2

35   data are sparse. Through a case study, in which the spatial distribution of the annual $^{13}CO_2$

36   discrimination rate over land is ignored by treating it as a constant at the global average of -14.1‰,

37   the spatial distribution of the inverted CO_2 flux over land was found to be significantly modified (up

38   to 15% for some regions). The uncertainties in our disequilibrium flux estimation are 8.0 PgC y^{-1}‰

39   and 12.7 Pg C y^{-1}‰ for land and ocean, respectively. These uncertainties induced uncertainties of

40   0.47 Pg C y^{-1} and 0.54 Pg C y^{-1} in the inverted CO_2 fluxes for land and ocean, respectively. Our joint

41   inversion system is therefore useful for improving the partitioning between ocean and land sinks and

42   the spatial distribution of the inverted carbon flux.

1. Introduction

Over the last few decades, much progress has been made in estimating the global carbon cycle using different methods (*Houghton et al.*, 2007; *Canadell et al.*, 2007; *Le Quéré et al.*, 2013). In particular, atmospheric CO_2 mole fractions measured near the surface have been used to infer the carbon flux over land and ocean surfaces through atmospheric inversion (*Rödenbeck et al.*, 2003; *Michalak et al.*, 2005; *Peylin et al.*, 2005; *Peters et al.*, 2007). However, the uncertainty in the inferred flux is still very large, mostly because of the insufficient number of observation stations and the error in modeling the atmospheric transport of CO_2 from the surface to the observation stations. To reduce this uncertainty, it would be useful to introduce constraints to the inversion using other gas species that are associated the CO_2 flux.

Measurements of the atmospheric concentration of the stable isotope $^{13}CO_2$ at a number of stations across the globe since 1994 have been compiled in a database (*GLOBALVIEW-CO2C13*, 2009), and the number of extended $^{13}CO_2$ records from January 1994 to January 2009 increased to 76 by 2009. The mole fraction of $^{13}CO_2$ to CO_2 in the atmosphere is about 1.1%, and the CO_2 exchange between the surface and the atmosphere generally induces concurrent $^{13}CO_2$ exchange. However, the proportion of the $^{13}CO_2$ flux relative to the CO_2 flux differs at different locations and different times due to different mechanisms that discriminate against heavier $^{13}CO_2$ molecules in the exchange processes, and therefore the $^{13}CO_2$ concentration measured in the atmosphere contains additional information for the CO_2 flux. This information is useful for differentiating between terrestrial and oceanic CO_2 exchanges with the atmosphere because the terrestrial CO_2 flux experiences much greater discrimination against $^{13}CO_2$ than does the oceanic CO_2 flux (*Tans et al.*, 1990; *Ciais et al.*,

65 1995a; *Francey et al.*, 1995). Observed $^{13}CO_2$ mole fractions can also provide independent

66 information on the net CO_2 exchange over land and ocean because the net carbon flux to the surface

67 discriminates against heavier $^{13}CO_2$ (*Fung et al.*, 1997; *Randerson et al.*, 2002; *Suits et al.*, 2005).

68 The $^{13}CO_2$ observations over the globe, albeit with a limited number of stations, could therefore be

69 used to assist in quantifying the global carbon cycle.

70   In previous studies (*Siegenthaler and Oeschger*, 1987; *Keeling et al.*, 1989a; *Francey et al.*,

71 1995; *Randerson et al.*, 2002), atmospheric $^{13}CO_2$ observations have been used to separate ocean and

72 land CO_2 fluxes through the use of a technique dubbed "double deconvolution", by which the CO_2

73 fluxes of land and ocean are separated (deconvolved) based on different discrimination rates against

74 $^{13}CO_2$ in the atmospheric CO_2 exchange with land and ocean surfaces. This double deconvolution

75 often assumes that the discrimination rates over land and ocean are spatially uniform, although they

76 can be temporally variable. Through forward atmospheric transport modeling, the ocean and land

77 CO_2 fluxes were also separated based on the spatial gradients of the measured $^{13}CO_2$/CO_2 ratio either

78 globally (*Keeling et al.*, 1989b) or by latitudinal bands (*Ciais et al.*, 1995a). The same $^{13}CO_2$ data

79 have also been used in inverse modeling of the surface CO_2 flux (*Enting et al.*, 1995; *Rayner et al.*,

80 1999; *Rayner et al.*, 2008). *Enting et al.* (1995) pioneered a methodology for inverting annual mean

81 ocean and land CO_2 fluxes from both atmospheric CO_2 and $^{13}CO_2$ concentration data for 12 ocean

82 regions and 8 land ecosystems for the 1986-1987 and 1989-1990 periods. *Rayner et al.* (1999)

83 developed a different methodology to invert monthly CO_2 fluxes for 12 ocean and 14 land regions for

84 the period from 1980 to 1995 from CO_2 observations at 12 stations and $^{13}CO_2$ and O_2/N_2

85 observations at 1 station. *Rayner et al.* (2008) refined their methodology and applied it to the period

86 from 1992 to 2005 using CO_2 at 67 sites and $^{13}CO_2$ at 10 sites. These studies showed the usefulness

87 of the additional information from $^{13}CO_2$ observations in improving the inversion of annual mean and

88 seasonality of the CO_2 flux over land and ocean. In these inversion studies, the discrimination rate for

89 land is either assumed to be a constant (*Enting et al*., 1995; *Rayner et al*., 1999) or allowed to vary

90 with the areal fraction of C4 plant in a region (*Rayner et al*., 2008). These inversions based on the

91 Bayesian principle were also constrained with only simple prior estimates of the terrestrial and

92 oceanic CO_2 and $^{13}CO_2$ fluxes. Since the data density (the numbers of CO_2 and $^{13}CO_2$ observation

93 sites) is low, the assumed discrimination constants and these prior estimates would have considerable

94 influence on the inverted results, as this is clearly demonstrated in *Enting et al*. (1995).

95   Atmospheric CO_2 observations have been extensively used to estimate the carbon flux over

96 ocean and land through inverse modeling using Bayesian synthesis (*Gurnay et al., 2002; Rödenbeck

97 et al.,2003; Baker et al., 2006; Peylin et al. 2005*) or data assimilation techniques (*Peters et al., 2007;

98 Zhang et al.*, 2014). Atmospheric inversion studies (*Gurnay et al.*, 2003; *Jacobson et al.*, 2007) often

99 produced ocean sinks considerably smaller than those estimated based on observed gradients in

100 dissolved inorganic carbon (DIC) in interior ocean using ocean circulation models (*Steinkamp and

101 Gruber*, 2013). Recent estimates for the ocean sink for anthropogenic CO_2 in 2000's based on DIC

102 ranges from 1.6 to 2.6 Pg C y^{-1} (*Park et al*., 2010; *Wanninkhof et al*., 2013; *Landschützer et al.*, 2014;

103 *Majkut et al.*, 2014; *DeVries*, 2014; *Rödenbeck et al.,* 2014) with an uncertainty of about 0.6 Pg C y^{-1},

104 while atmospheric inversion results are not yet reliable enough to be included in a global ocean sink

105 synthesis (*Le Quéré et al*., 2013). The partition between ocean and land fluxes using atmospheric

106 inversion techniques is sensitive to errors in atmospheric transport modeling (*Baker et al.,* 2006;

107 *Stephens et al.,* 2007) and prior fluxes for land and ocean used to constrain the inversion (*Zhang et

108 al., 2014; Chen et al.,* 2015). It would therefore be highly desirable to use $^{13}CO_2$ observations to

109 constrain this partition in the inversion process. Accurate partition between ocean and land sinks is

110 important in global carbon cycle research because (1) land sinks are still more reliably estimated as

111   the residual of the global carbon budget than those from land-based data (*Le Quéré et al.*, 2013) and

112   (2) ocean sink estimates based on DIC in ocean water also suffer from considerable errors due to

113   insufficient DIC observations and in ocean circulation modeling (*DeVries*, 2014).

114   The overall goal of this study is to explore the information content of $^{13}CO_2$ measurements

115   for global CO_2 flux estimation through developing a Bayesian synthesis inversion system that uses

116   both CO_2 and $^{13}CO_2$ observations. This system is effectively a new double de-convolution system

117   with the capacity to consider the spatial variations of the prior carbon flux and all major isotopic

118   parameters including photosynthetic discrimination, respiratory signature, and disequilibrium rate. In

119   this study, this new system is used to achieve the following objectives: (1) to partition between ocean

120   and land sinks with consideration of the spatial distributions of $^{13}CO_2$ isotopic parameters over ocean

121   and land; (2) to evaluate the importance of considering the spatial distributions of the $^{13}CO_2$

122   discrimination rate over land in the inversion of the CO_2 flux, and (3) to assess the impacts of the

123   errors in disequilibrium flux estimation on the flux partition between ocean and land. To achieve

124   these objectives, a terrestrial ecosystem model named the Boreal Ecosystem Productivity Simulator

125   (BEPS) is further developed to simulate the spatial distributions of the $^{13}CO_2$ discrimination and

126   disequilibrium rates over land for use in a global Bayesian synthesis inversion with $^{13}CO_2$ constraint.

127   BEPS is also used to produce CO_2 prior fluxes globally to regularize the inversion.

128   **2. Methodology**

129   **2.1 The inversion method**

130   2.1.1   Inversion system

131   The nested inversion system with a focus on North America developed by *Deng et al.* (2007)

132   is adopted in this study. In this system, two of the Transcom regions (*Gurney et al.*, 2002) in North

133   America are divided into 30 regions according to ecosystem types and administrative boundaries

134   (Figure 1), in order to reduce spatial aggregation errors in the inversion over North America and to

135   investigate the inverted spatial distribution of the carbon flux against ecosystem model results. This

136   nested region serves the purpose of evaluating the influence of the spatial distribution of isotopic

137   discrimination on the inverted carbon flux at a relatively high resolution. Also shown in Figure 1 are

138   the spatial distributions of 210 CO_2 and 73 $^{13}CO_2$ observation sites selected in this study from the

139   NOAA GLOBALVIEW database. Most $^{13}CO_2$ sites except 11 are collocated with CO_2 sites.

2.1.2   Synthesis Bayesian inversion with CO_2 observations

141   To estimate the CO_2 flux ($\mathbf{f}$), we represent the relationship between CO_2 measurements and

142   the flux from the surface by a linear model:

143        $$\mathbf{c} = \mathbf{G}\mathbf{f} + \mathbf{A}c_0 + \boldsymbol{\varepsilon} \tag{1}$$

144   where $\mathbf{c}_{m \times 1}$ is a given vector of m CO_2 concentration observations over space and time (m equals

145   number of stations times number of months, and for CO_2 only inversion, it is 12600, i.e. 210 stations

146    $\times$ 60 months, 2000-2004); $\boldsymbol{\varepsilon}_{m \times 1}$ is a random error vector with a zero mean and a covariance matrix

147    $\mathrm{cov}(\boldsymbol{\varepsilon}) = \mathbf{R}_{m \times m}$; $\mathbf{G}_{m \times (n-1)}$ is a matrix representing a transport (observation) operator, where n-1 is the

148   number of fluxes to be determined (equals 3000, i.e. 50 regions $\times$ 60 months, 2000-2004); $\mathbf{A}_{m \times 1}$ is a

149   unity vector (filled with 1) representing the assumed initial well-mixed atmospheric CO_2

150   concentrations (c_0) before the first month; and $\mathbf{f}_{(n-1) \times 1}$ is an unknown vector of monthly carbon

151   fluxes of the 50 regions.

152   Combining matrixes $\mathbf{G}$ and $\mathbf{A}$ as $\mathbf{M}_{m \times n} = (\mathbf{G}, \mathbf{A})$ and vectors $\mathbf{f}$ and c_0 as $\mathbf{s}_{n \times 1} = (\mathbf{f}^T, c_0)^T$, eq.

153   (1) can be expressed as

154 $$\mathbf{c} = \mathbf{Ms} + \boldsymbol{\varepsilon}$$ (2)

155   The inverse problem of estimating $\mathbf{s}$ from $\mathbf{c}$ is often poorly constrained and a Bayesian

156 approach is used to circumvent this problem. Pre-existing knowledge and models incorporating

157 additional sources of information can be used to provide an initial estimate of $\mathbf{s}$, known as the *a*

158 *priori*, to constrain the inversion. This *a priori* is then updated when it is combined with information

159 from $\mathbf{c}$ measurement to form a posterior estimate of $\mathbf{s}$, known as the *a posteriori*. In Bayesian

160 synthesis inversion (*Tarantola*, 1987), the following objective function is employed in the place of

161 the traditional least square objective function:

162 $$J = \frac{1}{2}(\mathbf{Ms} - \mathbf{c})^{\mathbf{T}}\mathbf{R}^{\mathbf{-1}}(\mathbf{Ms} - \mathbf{c}) + \frac{1}{2}(\mathbf{s} - \mathbf{s_p})^{\mathbf{T}}\mathbf{Q}^{\mathbf{-1}}(\mathbf{s} - \mathbf{s_p})$$ (3)

163 where $\mathbf{s}_{\mathbf{p}n\times1}$ is the *a priori* estimate of $\mathbf{s}$; the covariance matrix $\mathbf{Q}_{n\times n}$ represents the uncertainty in the

164 *a priori* estimate; and $\mathbf{R}_{m\times m}$ is the transport model-data mismatch error covariance. By minimizing

165 this objective function expressed in eq. (3), we obtain the posterior best estimate of $\mathbf{s}$ as [*Enting*,

166 2002]:

167 $$\hat{\mathbf{s}} = (\mathbf{M}^{\mathbf{T}}\mathbf{R}^{\mathbf{-1}}\mathbf{M} + \mathbf{Q}^{\mathbf{-1}})^{\mathbf{-1}}(\mathbf{M}^{\mathbf{T}}\mathbf{R}^{\mathbf{-1}}\mathbf{c} + \mathbf{Q}^{\mathbf{-1}}\mathbf{s_p})\,.$$ (4)

168 Meanwhile the posterior uncertainty matrix for the posterior flux can be deduced as follows:

169 $$\hat{\mathbf{Q}} = (\mathbf{Q}^{\mathbf{-1}} + \mathbf{M}^{\mathbf{T}}\mathbf{R}^{\mathbf{-1}}\mathbf{M})^{\mathbf{-1}}\,.$$ (5)

170

171   Following the methodology of Deng and Chen (2011), the CO_2 concentration matrix $\mathbf{c}$ in the

172 above equations is the residual concentration after subtracting the observed concentration with

173 contributions from fossil fuel emission, biomass burning, the prior ocean flux and the prior

174 biospheric flux (see Section 2.4 for detail). In this way, the values in $\mathbf{s_p}$ are set to zero and the

175 inverted flux $\mathbf{s}$ is considered to be an adjustment to the prior flux that contributes to the pre-

176 subtracted portions of the CO_2 concentration.

2.1.3   Synthesis Bayesian inversion with both CO_2 and $^{13}CO_2$ observations

178   We attempt to use $^{13}CO_2$ observations to provide an additional constraint to the otherwise

179 CO_2-only inversion presented above. This additional constraint is possible on the grounds that air

180 $^{13}CO_2$ concentration is affected differently by carbon fluxes from ocean and land surfaces. Since the

181 $^{13}CO_2$ gas is transported passively in similar ways as CO_2, the same transport matrix $\mathbf{M}$ applies to

182 $^{13}CO_2$ data to associate $^{13}CO_2$ observations with the surface $^{13}CO_2$ flux. This simple treatment of the

183 transport matrix differs from Rayner et al. (2008) who considered the reduced response of observed

184 $^{13}CO_2$ concentrations to surface fluxes with time due to its accumulated exchange with the surface.

185 As we are interested in the net CO_2 flux, the exchanges of both $^{13}CO_2$ and CO_2 with the surface are

186 consistently not included in the M matrix calculation, although this simplification would induce

187 errors in the inverted CO_2 flux when the accumulated exchanges are spatially highly heterogeneous.

188 In order to conduct an inversion using both CO_2 and $^{13}CO_2$ observations, we simply append $^{13}CO_2$-

189 related data to the $\mathbf{c}$, $\mathbf{R}$ and $\mathbf{M}$ matrixes in Eq. (4), while the $\mathbf{s}$ matrix remains unchanged as the

190 purpose of this joint inversion is only to optimize the CO_2 flux. For $\mathbf{c}$ and $\mathbf{R}$, $^{13}CO_2$ observations and

191 their variances are appended directly to the original matrixes for the CO_2 only case, as shown in Eq.

192 6. Similarly, the $\mathbf{M}$ matrix is also extended to consider $^{13}CO_2$ transport, and the relevant elements for

193 the $^{13}CO_2$ observation stations are from the original $\mathbf{M}$ matrix. However these elements are

194 multiplied by the $^{13}CO_2$ discrimination rate over land or ocean for each region and each month in

195 order to relate the CO_2 flux to the temporal variations in the measured air $^{13}CO_2$ composition at each

196 station and each month. The extended **M** is a combination of the corrected **M** matrix appended to the

197 **M** matrix for CO_2 (see below)

$$
\begin{bmatrix}
M_{1,1} & M_{1,2} & \cdots\cdots & M_{1,n} \\
M_{2,1} & M_{2,2} & \cdots\cdots & M_{2,n} \\
\multicolumn{4}{c}{\cdots\cdots} \\
M_{m,1} & M_{m,2} & \cdots\cdots & M_{m,n} \\
W_{m+1,1} & W_{m+1,2} & \cdots\cdots & W_{m+1,n} \\
W_{m+k,1} & W_{m+k,2} & \cdots\cdots & W_{m+k,n}
\end{bmatrix}
\begin{bmatrix}
S_1 \\ S_2 \\ \\ \\ \\ S_n
\end{bmatrix}
=
\begin{bmatrix}
C_1 \\ C_2 \\ \\ C_m \\ C_{m+1} \\ C_{m+k}
\end{bmatrix}
$$

All available CO_2 data

73 stations' ^{13}C data

198 (6)

199 where c_i is the CO_2 concentration (i=1 to m) and ^{13}C composition (i=m+1 to m+k) in the air from the

200 starting month (i=0); M_{ij} is the transport operator between region-month j (hereafter simply referred

201 as region) and station-month i (hereafter simply referred as station), and $W_{ij} = D_j M_{ij}$, in which D_j is

202 the discrimination rate against $^{13}CO_2$ in the CO_2 flux for region j. In the inversion procedure, the

203 difference in concentration between two consecutive times is equated with the flux during the time

204 interval (one month).

205   In order to calculate D_j and C_i (i=m+1 to m+k) in Eq. 6, some theoretical development is

206 made according to the $^{13}CO_2$ budget equation derived by Tans et al. (1993):

207 $C_a \dfrac{d\delta_a}{dt} = F_f(\delta_f - \delta_a) - (F_{lph} - F_{lb})\varepsilon_{lph} + F_{lb}(\delta_{lb} - \delta_{lb}^e) - (F_{oa} - F_{oa})\varepsilon_{ao} + F_{oa}(\delta_a^e - \delta_a)$ (7)

208 where C_a is the CO_2 pool in the atmosphere (in Pg C), δ_a is the ^{13}C composition of the atmosphere

209 in ‰, F_f is the carbon emission from fossil fuels and biomass burning, δ_f is the ^{13}C composition of

210 fossil fuels or biomass, F_{lph} is the photosynthetic carbon uptake by the land biosphere (always

211 positive), F_{lb} is the respiratory carbon flux of the land biosphere (always positive), ε_{lph} is the

212 photosynthetic discrimination of the land biosphere in ‰, δ_{lb} is the ^{13}C composition of the land

213   respiratory carbon flux (see Section 2.2.2), δ_{lb}^e is the biospheric ^{13}C composition in equilibrium with

214   the current atmosphere (i.e. in 2003), F_{oa} is the one-way carbon from the ocean surface to the

215   atmosphere (always positive), F_{ao} is the one-way carbon flux from the atmosphere to the ocean

216   surface (always positive), ε_{ao} is the air-to-ocean fractionation, ε_{oa} is the air-to-ocean fractionation,

217   and δ_a^e is the ^{13}C composition in equilibrium with the ocean surface. Eq. 7 states that the temporal

218   variation of the measured ^{13}C composition in the atmospheric CO_2 is determined by contributions

219   from the various sources: fossil fuels and biomass burning (term 1 of the right hand side of Eq. 7),

220   net land biosphere carbon uptake (term 2), one-way respiratory flux from the land biosphere (term 3),

221   net carbon flux of the ocean (term 4), and one-way ocean-to-atmosphere flux (term 5). The one-way

222   carbon fluxes from land and ocean surfaces are important sources of ^{13}C because the atmosphere is in

223   isotopic disequilibrium with these surfaces due to the long-term change of the atmospheric ^{13}C

224   composition. Similar to other terms in Eq. 7, these disequilibrium fluxes are also called isofluxes

225   (*Rayner*, 2001).

226   In order to reduce the errors of our inversion system (Eq. 6) that assumes linear relationships

227   between fluxes and concentrations, the contributions of all fluxes, including prior biospheric and

228   ocean fluxes, to the CO_2 concentration are subtracted from the measured CO_2 concentration prior to

229   the inversion (*Deng and Chen*, 2011). Accordingly, the contributions of all ^{13}C sources to the ^{13}C

230   concentration in the atmosphere are also subtracted from the measured ^{13}C concentration. The

231   purpose of the inversion is then to find the residual CO_2 flux, denoted as **S** in Eq. 6. For this purpose,

232   we denote $S_{lN} = -(F_{lph}-F_{lb})$ as the net flux from the land surface to the atmosphere (negative for sinks)

233   and $S_{oN} = -(F_{ao}-F_{oa})$ as the net flux from the ocean surface to the atmosphere (negative for sinks).

234   After taking $S_{lN} = S_{lN}^P + S_l$ and $S_{oN} = S_{oN}^P + S_o$, where S_{lN}^P and S_{oN}^P are the prior net CO_2 fluxes to the

235   land and ocean surfaces, respectively, and S_l and S_o are the residual fluxes to be inverted for the land

236   and ocean surfaces, respectively, Eq. 7 can be rewritten as:

237      $$S_l \varepsilon_{lph} + S_o \varepsilon_{ao} = C_a \frac{d\delta_a}{dt} - [F_f(\delta_f - \delta_a) + S_{lN}^P \varepsilon_{lph} + F_{lb}(\delta_{lb} - \delta_{lb}^e) + S_{oN}^P \varepsilon_{ao} + F_{oa}(\delta_a^e - \delta_a)] \qquad \textbf{(8)}$$

238   Eq. 8 is the theoretical basis for our joint $^{13}C/^{12}C$ inversion as it links the measured ^{13}C composition

239   in the atmosphere to the CO_2 fluxes of the land and ocean surfaces. In the implementation of the joint

240   inversion system (Eq. 6), a transport matrix is used to link a flux in a particular region to the

241   concentration measured at a particular site. We focus on optimizing the net CO_2 flux using both CO_2

242   and $^{13}CO_2$ observations rather than optimizing the one-way fluxes, and therefore the discrimination

243   terms to be optimized are moved to the left-hand side of Eq. 8 and the disequilibrium terms remain

244   on the right-hand side. Based Eq. 8, the regional discrimination D_j in Eq. 6 is therefore defined as:

245
$$\begin{aligned} D_j &= \varepsilon_{lph,j} \quad \text{for land} \\ D_j &= \varepsilon_{ao,j} \quad \text{for ocean} \end{aligned} \qquad\qquad (9)$$

246   where $\varepsilon_{lph,j}$ and $\varepsilon_{ao,j}$ are the ^{13}C fractionation ratio for region j for land and ocean fluxes,

247   respectively. In the joint inversion system, we treat S_l and S_o as the state variables and D_j as

248   predetermined parameters that vary in space (region) and time (monthly). It is therefore prerequisite

249   to estimate accurately these parameters as well as other isotopic parameters on the right hand side of

250   Eq. 8.

251   For land regions, BEPS is used to calculate all land variables in Eq. 8, including S_{lN}^P, F_{lb}, ε_{lph},

252   R_{lb}, δ_{lb} and δ_{lb}^e for each region and month. For ocean regions, ε_{ao}=-2‰, and empirical equations

253   developed by *Ciais et al.* (1995b) are used to calculate F_{oa} and δ_a^e as functions of sea surface

254   temperature on 1°×1° grids.

255   The $^{13}CO_2$ concentration time series ($c_{m+1}, ... c_{m+k}$) in Eq. 6 in ppm‰ is the numerical

256   realization of the right hand side of Eq. 8 and is computed with the following equation:

257
$$c_i = \overline{C}_{a,i} \frac{d\delta_{a,i}}{dt} - \sum_{k=1}^{5} {}^{13}\delta_k \frac{dC_{k,i}}{dt}$$
(10)

258   In Eq.10, $\overline{C}_{a,i} \dfrac{d\delta_{a,i}}{dt}$ can be calculated with observed CO_2 concentration and ^{13}C composition at two

259   consecutive times, t and $t+1$, using the following equation:

260
$$\overline{C}_{a,i} \frac{d\delta_{a,i}}{dt} = \frac{C_{a,i}^{t+1} + C_{a,i}^{t}}{2} (\delta_{a,i}^{t+1} - \delta_{a,i}^{t})$$
(11)

261   where $\overline{C}_{a,i}$ is the mean concentration of CO_2 at each observation station i between t and $t+1$, and

262    $\delta_{a,i}$ is the ^{13}C composition at station i, and its derivative with time is taken as its difference between t

263   and $t+1$. This derivative represents the δ_a growth rate that is the combined outcome of the various

264   isofluxes in Eq. 7. The term $\sum_{k=1}^{5} {}^{13}\delta_k \dfrac{dC_{k,i}}{dt}$ is the sum of $^{13}\delta$ changes due to fossil fuel and biomass

265   burning, prior land ^{13}C discrimination flux, land ^{13}C disequilibrium flux, prior ocean ^{13}C

266   discrimination flux, ocean ^{13}C disequilibrium flux, corresponding to the terms in Eq.8. $^{13}\delta_k$

267   represents $^{13}\delta$ value (‰) for each term in Eq.8, and $\dfrac{dC_{k,i}}{dt}$ is the change of concentration (ppm)

268   calculated with the flux of each term in Eq.8 according to the atmospheric transport function $\mathbf{M}$ in

269   Eq.6.

270   The uncertainty of c_i as part of the uncertainty matrix $\mathbf{R}$ includes the uncertainties of the six

271   terms on the right hand side of Eq. 10. The uncertainty for the first term is based on the measurement

272   error (see next Section 2.1.4) and its global average is 3.08 ppm‰/month. The uncertainties of terms

273   2 to 6 are estimated to be 0.95, 3.17, 0.87, 0.12, and 2.69 ppm‰/month, respectively. The total

274   uncertainty for c_i is therefore 5.33 ppm‰/month as a global average, taking as the square root of the

275   sum of the square of the six uncertainties. As an approximation, this total uncertainty is distributed to

276   each station and each month according to the spatial and temporal patterns of uncertainty of the first

277   term.

278   The inversion system defined by Eq. 6 can be implemented in three ways using (1) CO_2

279   concentration only by excluding the appended matrices for $^{13}CO_2$, (2) $^{13}CO_2$ data only by using

280    $^{13}CO_2$-related matrices only, and (3) both CO_2 and $^{13}CO_2$ data. Through using the data in these three

281   ways, the information content of $^{13}CO_2$ measurements for CO_2 can be systematically investigated.

282   In order to investigate the influences of the isotopic discrimination and disequilibrium over

283   land and ocean on the inversion results, we conduct five sets of inversions for the following cases:

284   Case I: The spatial variations of all isotopic compositions and the discrimination and disequilibrium

285   fluxes in Eq. 8 are considered for both land and ocean. This is the ideal case as the basis to

286   investigate other cases; Case II: The photosynthetic discrimination (ε_{lph}) over land is taken as a

287   constant of -14.1‰, which is the global average obtained by BEPS, and therefore D_j=-14.1‰. This is

288   a case to ignore regional differences in isotopic discrimination over land; Case III: All isotopic

289   variables are the same as Case I, but the land disequilibrium term in Eq. 8 is ignored. This is a case to

290   investigate the influence of the land isotopic disequilibrium on the CO_2 flux inversion; Case IV: All

291   isotopic variables are the same as Case I, but the ocean disequilibrium term in Eq. 8 is ignored. This

292   is a case to investigate the influence of the ocean isotopic disequilibrium on the CO_2 flux inversion;

293   and Case V: Both land and ocean disequilibrium terms are ignored, but all other isotopic variables in

294   Eq. 8 are same as Case I. This is a case to investigate the importance of the total disequilibrium flux

295   in CO_2 flux inversion at the global scale. Cases III to V are useful not only for evaluating the

296 performance of the joint inversion system but also for assessing the impacts of errors in isotopic

297 disequilibrium estimation on the CO_2 flux inversion.

2.1.4 Covariance matrixes for the CO_2 flux and CO_2 and $^{13}CO_2$ concentration measurements

300 In the joint inversion using both CO_2 and $^{13}CO_2$ measurements, the covariance matrix (**Q**) for

301 the CO_2 flux remains the same as that in the CO_2 only inversion (Eq. 3) but the error matrix (**R**) for

302 concentration measurements is expanded to the dimension of 16980×16980 to include 60 months of

303 $^{13}CO_2$ observations at 73 stations. Following *Deng and Chen* (2011), we use an uncertainty of 2.0 Pg

304 C y^{-1} for the total global land surface CO_2 flux, and this total uncertainty is spatially distributed to the

305 39 regions according to the annual total NPP of these regions simulated by BEPS. For each region,

306 the annual total uncertainty is further distributed to each month according to the simulated seasonal

307 variation in NPP. The global total uncertainty (standard deviation) is spatially and temporally

308 distributed in such a way that the total variance is preserved after the distributions, following the

309 principle of TRANSCOM 3 (Gurnay et al., 2003). The uncertainty for the total ocean flux is

310 prescribed as 0.67 Pg C y^{-1} (*Deng and Chen,* 2011). In this way, all the diagonal elements (Q_{ii}) in the

311 uncertainty matrix **Q** are determined, while off-diagonal values are assigned to zero, meaning that no

312 flux covariances between regions and months are assumed. The uncertainty of CO_2 measurements in

313 the **R** matrix is the same as that described in *Deng and Chen* (2011), following the approach of

314 *Peters et al*. (2005) and *Bakers et al*. (2006). In this approach, the uncertainty of a monthly CO_2

315 measurement at a site is estimated as $R_{ii} = \sigma_{const}^2 + GVsd^2$, where constant portion σ_{const} in ppm is

316 assigned according to site category: Antarctic (0.15) , oceanic (0.30), land and tower (1.25),

317 mountain (0.90), and aircraft (0.75), while the site-specific variable portion *GVsd* is obtained from

318   the GLOBALVIEW-CO2 2008 database. The $^{13}CO_2$ measurement uncertainty is calculated in a

319   similar way: the variable portion is obtained from the GLOBALVIEW-13CO2 2008 database, while

320   the constant portion is taken as $R_a\sigma_{const}$ in ppm first, where R_a is the ratio of $^{13}CO_2$ to CO_2 in the air

321   (~0.011147), and then converted to ‰. The average standard deviation of $\delta^{13}C$ observations

322   determined in this way for 73 stations is 0.0685‰.

323

324   **2.2 Prior CO_2 and $^{13}CO_2$ flux estimation**

325   **2.2.1 CO_2 flux**

326   **Terrestrial biosphere fluxes**

327   A process-based terrestrial ecosystem model called the Boreal Ecosystem Productivity Simulator

328   (BEPS) (*Chen et al.*, 1999; *Liu et al.*, 1997) is used in this study to estimate the net terrestrial CO_2

329   flux and its components including the gross primary productivity (GPP), net primary productivity

330   (NPP), heterotrophic respiration (F_{lb}), and net ecosystem productivity (NEP). GPP is calculated using

331   the Farquhar's leaf-level model (*Farquhar et al*, 1980) upscaled to the canopy level using a recently

332   refined two-leaf approach (*Chen et al*., 2012). NPP is taken as 45% of GPP (*Ise et al*., 2010) as

333   global biomass data and its components (stem, foliage, root) are lacking for reliable computation of

334   the autotrophic respiration. F_{lb} is calculated as the sum of the decompositional CO_2 release from 9

335   soil carbon pools, namely coarse and dead wood detritus pool, surface structural pool, surface

336   metabolic pool, surface microbial pool, fine-root structural litter pool, fine-root metabolic pool, soil

337   microbial pool, slow carbon pool, and passive carbon pool. The sizes of these pools for each cover

338   type in each 1° grid are estimated using a model spin-up approach based on simulated NPP in 2000 to

339   create a global land sink of 3.73 Pg C y^{-1}. The total NPP for each 1° grid is taken as a weighted sum

340 of NPP of 7 aggregated land cover types, and the weights are proportional to the areal fractions of the

341 cover types determined using the GLC2000 land cover map at 1 km resolution (*Chen et al.*, 2012).

342 Remotely sensed LAI [*Deng et al.*, 2006] at 1 km resolution and a clumping index map at 6 km

343 resolution (*Chen et al.*, 2005) and a soil textural map (*Webb et al.*, 1991) are aggregated to 1º grids

344 for each cover type based on GLC2000 land cover and used as input to BEPS. National Center of

345 Environmental Prediction (NCEP) reanalyzed data [*Kalnay et al.*, 1996; *Kanamittsu et al.*,2002] are

346 the meteorological drivers for BEPS to simulate hourly carbon fluxes. The output of BEPS used as

347 the prior flux in the inversions is NEP, which does not include carbon emission due to disturbance.

348 **Ocean fluxes**

349 The daily flux of CO_2 across the air-water interface used in this study is constructed based on

350 the results of daily CO_2 fluxes simulated by the OPA-PISCES-T model [*Buitenhuis et al.*, 2006].

351 This model is a global ocean general circulation model (OPA) [*Madec et al.*, 1998] coupled to an

352 ocean biogeochemistry model (PISCES-T) [*Aumont et al.*, 2003; *Buitenhuis et al.*, 2006]. PISCES-T

353 represents the full cycles of C, O_2, P, Si, total alkalinity and a simplified Fe cycle. It also includes a

354 representation of two phytoplankton, two zooplankton and three types of dead organic particles of

355 different sinking rates. OPA-PISCES-T is forced by daily wind stress and heat and water fluxes from

356 the NCEP reanalyzed data [*Kalnay et al.*, 1996, *Kanamittsu et al.,2002]*. Hourly S_o (^{13}C) is calculated

357 with gridded optimum interpolation sea surface temperature of NOAA National Climate Data Center

358 (*Reynolds and Smith*, 1994; *Reynolds et al.*, 2002).

359 **Fossil-fuel emissions**

360 The fossil fuel emission field (2000-2004) used in this study (http://carbontraacker.noaa.gov)

361 is constructed based on (1) the global, regional and national fossil-fuel CO_2 emission inventory from

362 1871 to 2006 (CDIAC) [*Marland et al.*, 2009], and (2) the EDGAR 4 database for the global annual

363   CO_2 emission on a 1° grid [*Olivier et al.*, 2005]. The $^{13}CO_2$ flux from fossil-fuel consumption is

364   calculated from CO_2 emissions of different fuel types multiplied by their respective $^{13}C/^{12}C$ ratios

365   with consideration of their latitudinal distributions based on *Andres et al.* (2000).

Fire emissions

367   CO_2 emissions due to vegetation fires are an important part of the carbon cycle [*van der Werf*

368   *et al.*, 2006]. Each year, vegetation fires emitted around or more than 2 PgC of CO_2 into the

369   atmosphere, mostly in the tropics. The fire emission field used in this study is based on the Global

370   Emissions Fire Database version 2 (GFEDv2) (*Randerson et al.*, 2007; *van der Werf et al.*, 2006)

371   **2.2.2 $^{13}CO_2$ flux**

372   Based on the initial work of *Chen et al*. (2006), BEPS is further developed to include a

373   capacity to compute the global distribution of the terrestrial $^{13}CO_2$ flux. Following the principle of

374   multi-stage ^{13}C fractionation in the pathway through leaf boundary layer, stomates, messophyll and

375   chloroplast initially proposed by *Farquhar et al*. (1984,   1989) and implemented globally by *Suits et*

376   *al*. (2005), we developed a module in BEPS for computing the total photosynthetic fractionation and

377   the resultant $^{13}CO_2$ flux. Specifically, the photosynthetic discrimation for C3 plants (Δ_{PC3}) is

378   calculated from

$$\Delta_{PC3} = \frac{pA}{C_a}\left[\frac{\Delta_b}{g_b} + \frac{\Delta_s}{g_s} + \frac{\Delta_{diss} + \Delta_{aq}}{g_m}\right] + \frac{C_c}{C_a}\Delta_f \tag{12}$$

380   where Δ_b, Δ_s, Δ_{diss}, Δ_{aq}, and Δ_f are the rates of discrimination against $^{13}CO_2$ through leaf boundary

381   layer, stomates, dissolution in mesophyll water, transport in aqueous phase, and fixation in

382   chloroplast, respectively, and are assigned values of 2.9‰, 4.4‰, 1.1‰, 0.7‰ and 28.2‰,

383   respectively (*Suits et al*., 2005). A is the photosynthetic rate in mol m^{-2} s^{-1} and p equals to

384    $0.022624T_a/(273.16P)$ with the dimension of m^{3}mol^{-1}, where T_a is air temperature in °K and P is the

385 standard air pressure at 1.013Bar. C_a and C_c are the CO_2 concentrations in mol mol^{-1} in the free air

386 and leaf chloroplast, respectively. For C4 plants, the photosynthetic discrimination (Δ_{PC4}) is taken as

387 a constant of 4.4‰ (*Suits et al.*, 2005).

388   The leaf boundary-layer (g_b) is calculated with the following equation

389 $$g_b = \frac{\alpha N}{0.5l}$$ (13)

390 where α is the diffusivity of CO_2 in dry air in m^{2}s^{-1} calculated as $10^{-6}(0.129+0.007T_a)$ and T_a is the

391 air temperature in ℃; l is the leaf characteristic dimension in m, taken as a constant of 0.1 m; and N

392 is the Nusselt number equal to $(u_d l/\upsilon)^{0.5}$, where u_d is the wind speed in m s^{-1}at the vegetation

393 displacement height (80% of the average vegetation height) and υ is the kinematic viscosity of dry air

394 in m^2 s^{-1} calculated as $10^{-6}(0.133+0.007T_a)$. u_d is derived from the wind speed above the canopy

395 based on LAI and vegetation height assigned according to plant functional type (Table 1).

396   As part of the GPP calculation, the stomatal conductance (g_s) computed separately for sunlit

397 and shaded leaves using the Ball-Berry equation (Ball, 1988),

398 $$g_s = f_w(m\frac{A\,h_s}{C_s}p+b)$$ (14)

399 where f_w is a scaling factor depending on soil moisture and texture (*Chen et al.*, 2012); h_s is the air

400 humidity at the leaf surface; C_s is the CO_2 concentration at the leaf surface; p is the same as in Eq. 12;

401 and m and b are the slope and intercept in this linear relationship, and they are assigned values

402 according to plant function type (Table 1) (*Chen et al.*, 2012).

403   The mesophyll conductance g_m is calculated based on the method of Harley (1992):

404 $$g_m = \frac{A}{C_i - \frac{\Gamma \cdot [J + 8 \cdot (A + R_d)]}{J - 4 \cdot (A + R_d)}}$$ (15)

where A is the photosynthetic CO_2 assimilation rate; C_i is partial pressure of CO_2 in the air spaces

inside leaves; R_d is the respiration rate occurring during the day not related to photorespiration; Γ is

the CO_2 compensation point in the absence of R_d; and J is the rate of photosynthetic electron

transport. These parameters are the same as those used in computing the CO_2 flux.

Our methods of computing stomatal and mesophyll conductances differ from previous studies

(*Suits et al*., 2005; *Scholz et al*., 2008; *Rayner et al*., 2008) in the following ways: (1) these

conductances are calculated separately for sunlit and shaded leaves because BEPS is a two-leaf

model, in which the total GPP of a canopy is taken as the sum of sunlit and shaded leaf GPP; and (2)

the mesophyll conductance mechanistically depends on a set of parameters rather than being treated

as a constant or to be proportional to the stomatal conductance. Since it has been demonstrated that

sunlit and shaded leaf separation is essential for accurate modeling of canopy-level photosynthesis

(*Chen et al*., 1999; *Sprintsin et al*., 2011), it is expected that this separation is also essential for $^{13}CO_2$

flux estimation. We found that the use of Harley's method for computing the mesophyll conductance

makes the calculated ^{13}C photosynthetic fractionation stable for its global application, while the

simpler method of treating the mesophyll conductance in proportion with the stomatal conductance

often incurs abnormally large or small values of ^{13}C photosynthetic fractionation.

The photosynthetic $^{13}CO_2$ flux is in disequilibrium with the respiratory $^{13}CO_2$ flux because of

the change in atmospheric $^{13}CO_2$ concentration since the preindustrial time (*Ciais et al*., 1995b; *Fung*

et al., 1997). The heterotrophic respiratory flux from the decomposition of organic matter of different

ages carries the memory of the past atmospheric $^{13}CO_2$ concentration, while the photosynthetic $^{13}CO_2$

flux is affected by the current atmospheric $^{13}CO_2$ concentration. The isotopic composition of each of

the 9 soil carbon pools ($\delta^{13}C_{soil,\ i}$) is estimated with following formula:

427 $$\delta^{13}C_{soil,\,i} = \delta^{13}C_a\,(2003 - \tau_i) - \varepsilon_{lph} \tag{16}$$

428 where $\delta^{13}C_a$ is the isotopic composition of carbon in atmosphere CO_2 in the past as determined by the

429 ice-cord record (*Francey et al.*, 1999); ε_{lph} is the annual mean of photosynthetic discrimation in

430 2003; and τ_i is the age of carbon pool i (Table 2) (*Ju et al.*, 2005). In the calculation of the mean age

431 of a carbon pool, we have considered the ages of various carbon pools at the time of entering the pool

432 (*Potter et al., 1993*), so that the mean age is considerably larger than the turnover time determined by

433 the decomposition rate (*Fung et al., 1997*). The mean $\delta^{13}C_{soil}$ is taken as the flux-weighted $\delta^{13}C_{soil,i}$

434 for the 9 carbon pools. The results of $\delta^{13}C_{soil}$ for the globe are shown in Figure 5. The ^{13}C

435 composition of the biosphere δ_{lb} in Eq. 8 is taken as the mean $\delta^{13}C_{soil}$, while the biospheric ^{13}C

436 composition δ_{lb}^e in equilibrium with the current atmosphere is taken as $\delta_a - \varepsilon_{lph}$.

437   The accuracy of the BEPS model in simulating atmospheric $^{13}CO_2$ concentration was

438 previously tested (*Chen et al., 2006; Chen and Chen,* 2007) against measurements over a boreal

439 forest at Fraserdale, Ontario, Canada (49°52'29.9''N, 81°34'12.3''W). Flask measurements of $\delta^{13}C_a$

440 were made 40 times in both daytime and nighttime on a tower at a height of 20 m during a 3-day

441 campaign on 21-23 July 1999. BEPS simulated these measurements with RMSE=0.34‰ and r^2=0.76.

442   **2.3 Transport modeling**

443   A transport-only version of the atmospheric chemistry and transport model TM5 (Krol et al.,

444 2003; Krol et al., 2005) is used for CO2 and 13CO2 transport modeling to produce a fully linear

445 operator on these fluxes. The spatial resolution of TM5 is 6°×4° for the globe and 3°×2° for North

446 America, and the atmosphere is divided vertically into 25 layers with 5 layers in the planetary

447 boundary layer. Tracer transport (advection, vertical diffusion, cloud convection) in TM5 is driven

448 by offline meteorological fields taken from the European Centre for Medium Range Weather

449   Forecast (ECMWF) model. All physical parameterizations in TM5 are kept the same as the ECMWF

450   formulation to achieve compatibility between them. The four background fluxes from terrestrial

451   ecosystems, oceans, fossil-fuel burning, and biomass burning are individually inputted to TM5 to

452   calculate the contributions of these fluxes to the atmospheric CO_2 and $^{13}CO_2$ concentrations. Since

453   the main purpose of this study is to develop a joint inversion system, only one transport model is

454   used, the transport matrix $\mathbf{M}$ is assumed to be free of errors.

2.4 CO_2 and $^{13}CO_2$ datasets

456   Monthly CO_2 and $^{13}CO_2$ concentration data from 2000 to 2004 are compiled from the

457   GLOBALVIEW CO_2 and $^{13}CO_2$ database. Though the GLOBALVIEW database consists of both

458   extrapolated and interpolated data that were created based on the technique devised by *Masarie and*

459   *Tans* [1995], we selected the synchronized and smoothed values of actual observations to compile

460   our concentrations datasets. Only direct measurements of CO2 from the GlobalView dataset are used

461   in our inversion after using a time-frequency weighting scheme (Deng and Chen, 2011). There are

462   5431 monthly data from 209 sites for 42 months used for CO2 (5431 out of 8778, i.e. 209×42), and

463   3066 monthly data from 73 sites for 13CO2 (i.e. 73×42 monthly data). Since the number of 13CO2

464   observation sites is much smaller than that of CO2 sites, all monthly data at 73 sites are used for

465   13CO2, and the missing 13CO2 data are filled with the reference data provided in the same

466   GlobalView dataset. The filled data may have introduced an additional error to the dataset as shown

467   in Figure 15b.

468   To minimize the nonlinear aggregation effects of the large regions (*Pickett-Heaps,* 2007), the

469   contributions of the four background fluxes are subtracted from the above monthly concentrations.

470   So the matrix $\mathbf{c}$ in Eqs. (3) and (4) is expressed as

471        $$\mathbf{c} = \mathbf{c}_{obs} - \mathbf{c}_{ff} - \mathbf{c}_{bio} - \mathbf{c}_{ocn} - \mathbf{c}_{fire}$$ (17)

472   where $\mathbf{c}_{obs}$ is the monthly CO_2 and $^{13}CO_2$ concentrations obtained from GLOBALVIEW, and $\mathbf{c}_{ff}$,

473    $\mathbf{c}_{bio}$, $\mathbf{c}_{ocn}$, and $\mathbf{c}_{fire}$ are simulated contributions of CO_2 and $^{13}CO_2$ concentrations from the terrestrial

474   biosphere, ocean, fossil-fuel, and fire fluxes, respectively.

475

476   **3. Results**

477   **3.1 Prior CO_2 and $^{13}CO_2$ fluxes**

478   Terrestrial ecosystem models integrate many sources of information, including vegetation

479   structure, soil, and meteorology, to estimate carbon exchange of the land surface with the atmosphere.

480   Prior CO_2 and $^{13}CO_2$ fluxes produced by a model can therefore provide indispensible constraints to

481   the otherwise ill-posed inversion based on CO_2 and $^{13}CO_2$ concentration observations alone.

482   Depending on the assigned relative magnitudes of the error matrixes of these observations and these

483   prior fluxes (i.e., **R** and **Q** in Eq. 3), these prior fluxes can have equal or even dominant importance

484   to these observations in the inversion results. We have therefore paid a great attention in modeling

485   these prior fluxes, in order to minimize the total inversion errors. Figure 2a shows an example of the

486   global terrestrial GPP distribution in 2003 modeled by BEPS. The total GPP in this year is 132±22

487   Pg C y^{-1} (*Chen et al*., 2012). This value is larger than some of the recent estimates, such as 123 Pg C

488   y^{-1} by *Beer et al*. (2010), mostly because the LAI values used as input to BEPS are generally larger

489   than those of the MODIS product (*Garrigues et al*., 2008). Our LAI values are larger because we

490   used a global clumping index map derived from a multi-angle satellite sensor POLDER (*Chen et al*.,

491   2005). Clumping increases shaded leaves which contributed about 35% to the total GPP globally.

492   Without considering this clumping effect, the shaded leaf area is underestimated, resulting in an

493   underestimation of the global GPP by 9% (*Chen et al.*, 2012). As the spatial distribution of clumping

494   is not uniform (boreal and tropical forests are most clumped and crops and grasses are least clumped),

495   this refinement in the GPP spatial distribution would have some effects on the inversion results

496   between regions.

497   The net ecosystem productivity (NEP), which is the difference between GPP and ecosystem

498   respiration modeled by BEPS, is shown in Figure 2b for 2003. Even though GPP has a large

499   uncertainty (globally 22 Pg C y^{-1} by BEPS), the uncertainty in NEP is much smaller (globally 2 Pg C

500   y^{-1} by BEPS) because a model spin-up approach is used to estimate the soil carbon pool sizes based

501   on a dynamic equilibrium assumption. Under this assumption, the annual heterotrophic respiration

502   (F_{lb}) equals annual NPP during the preindustrial period, and the soil carbon pool sizes are derived

503   from F_{lb} by solving a set of differential equations describing the decomposition and interactions

504   among the pools (*Govind et al.*, 2011). In this way, F_{lb} is forced to depend on NPP and the systematic

505   biases in GPP are not carried into NEP estimation. NEP is non-zero after the preindustrial period

506   because of the changes in climate and atmospheric composition (CO_2 and nitrogen) as well as

507   disturbance. In our regional modeling, both disturbance and non-disturbance effects are considered

508   for Canada (*Chen et al.*, 2003) and USA (*Zhang et al.*, 2012) forests. However, in our global model

509   spin-up from 1901 (taken as the end of preindustrial period) to 2000, only the non-disturbance effects

510   are considered because of lack of spatially explicit disturbance data outside of North America, while

511   carbon emission due to fire disturbance in the study period from 2000 to 2004 is considered

512   separately using the GFED dataset (*Randerson et al.*, 2007; *van der Werf et al.*, 2006). The prior net

513   CO_2 fluxes for the globe for the years 2002-2004 are given in Table 3 with inversion results with and

514   without the ^{13}C constraint.

515   The global distribution of the total photosynthetic discrimination ($\delta^{13}C_{pt} = \delta^{13}C_a - \Delta$) modeled

516   by BEPS is shown in Figure 3. Forests, such as those in North America, Russia, Europe, Amazon,

517   central Africa, central China and southeast Asia, generally have high photosynthetic discrimination

518   rates (>16‰), while grassland and cropland (in particular C4 grasses and crops) have low

519   discrimination rates. Also shown in Figure 3 is the ocean diffusive discrimination against $^{13}CO_2$. The

520   discrimination over ocean is much smaller than that over land. This difference between land and

521   ocean discrimination may be considered as the largest signal of $^{13}CO_2$ observations on the global

522   carbon cycle (*Tans et al.*, 1990; *Rayner et al.*, 2008) and is considered in our inversion using

523   different $^{13}CO_2$ discrimination rates for ocean and land regions (see Eq. 6).

524   To estimate the disequilibrium between photosynthetic and respiratory discrimination against

525     $^{13}CO_2$, the global distribution of the mean soil carbon age is computed after weighting the ages of the

526   9 soil carbon pools against their fluxes due to decomposition (Figure 4). Forests at high latitudes

527   have the soil carbon age of about 40-60 years, while the tropical forests have much lower values in

528   the range from 10 to 30 years. This latitudinal distribution pattern is mostly determined by soil

529   temperature. In low latitudes, high temperature induces fast turnovers of detritus and fast soil carbon

530   pools, while at high latitudes, low temperature maintains relatively large fractions of slow and

531   passive soil carbon pools. Cropland and grassland also have larger fractions of fast and detritus

532   carbon pools than forest cover types and therefore have younger soil carbon on average. This spatial

533   distribution of soil carbon age has a strong influence on the total respiratory discrimination against

534   ^{13}C ($\delta^{13}C_r$) calculated by BEPS (Figure 5). Respiration from older carbon at high latitudes carries the

535   memory of the older atmosphere with less $^{13}CO_2$ concentration and hence has lower discrimination

536   rates (larger $\delta^{13}C_r$ or smaller absolute value). However, respiration would mostly depend on the

537   photosynthetic discrimination rates as soil organic matter originates from photosynthetic production.

538   As a result, forested areas have higher respiratory discrimination rates (lower $\delta^{13}C_r$ or larger absolute

539   value). Most of the high values of $\delta^{13}C_r$ in Figure 5 are associated with large fractions of C4 plants

540   in the grid, such as the corn belt in the USA, cropland in northeast China, southern border of Sahara

541   desert, and southeast South America. The global distribution of the disequilibrium between

542   photosynthetic and respiratory discrimination, taken as the difference between Figure 3 and Figure 5,

543   is shown in Figure 6. The disequilibrium is the largest at high latitude boreal forests in North

544   America and Eurasia because their soil carbon is the oldest, as shown in Figure 4. The spatial

545   distribution pattern of the disequilibrium is similar to those of *Ciais et al.* (1995b) and *Fung et al.*

546   (1997) but the magnitude is larger because the date of our result in 2000 is more recent than these

547   two previous studies. As the time lapses, the atmosphere is getting lighter in terms of the isotopic

548   composition of CO_2 resulting from the increased air-borne CO_2 from fossil fuel consumption.   Also

549   shown in Figure 6 is the disequilibrium over the ocean estimated using the method of *Ciais et al.*

550   (1995b). This ocean disequilibrium has a large latitudinal gradient because of the gradients in sea

551   surface temperature gradient and the fluxes of CO_2 and $^{13}CO_2$. The spatial distribution in the

552   disequilibrium and the differences in disequilibrium between ocean and land may be considered to be

553   the secondary signal of $^{13}CO_2$ observations on the global carbon cycle. The effects of these

554   disequilibria on the carbon flux are considered in our inversion through presubtracting their

555   contributions to the measured $^{13}CO_2$ composition in Eq. 10.

556   **3.2 Inverse modeling results**

557   Although the inversions were made for the 2000-2004 period, the results of the first two years are not

558   included in the analysis because they are affected by the assumption of uniform global distributions

559 of CO_2 and $^{13}CO_2$ concentrations at the start of our transport modeling using TM5. An 18-24 month

560 period is usually considered to be necessary for the simulated distributions to reach realistic states

561 with reasonably accurate prior surface fluxes from ocean and land and atmospheric transport

562 simulations (*Rödenbeck et al*., 2003; *Deng and Chen*, 2011). The following results are therefore

563 summarized as the average for the 2002-2004 period.

564 3.2.1 Partition between ocean and land sinks with and without $^{13}CO_2$ constraint

565   To investigate the usefulness of $^{13}CO_2$ observations in partitioning between ocean and land

566 sinks, we conducted inversions with and without $^{13}CO_2$ constraint as expressed in Eq. 6, i.e. with and

567 without the ^{13}C-related expansions of the matrixes. The CO_2-only inversion increases the land sink

568 from the prior of 2.61 PgC y^{-1} to 3.40 PgC y^{-1} while decreasing the ocean sink from the prior of 2.13

569 PgC y^{-1} to 1.48 PgC y^{-1} (Table 3). These results are similar to those of *Deng and Chen* (2011). The

570 results from the joint inversion are considerably different: the posterior sinks for land and ocean

571 become 2.53 and 2.36 PgC y^{-1} (Table 3), respectively, suggesting that the use of $^{13}CO_2$ observations

572 in the inversion considerably influenced the partition between land and ocean fluxes. The ratio

573 between land and ocean sinks is 1.07. The joint inversion system developed in this study may be

574 regarded as a different form of double deconvolution. Using the double deconvolution method with

575 the global average disequilibrium coefficients of 0.49‰ and 0.78‰ and the disequilibrium fluxes of

576 26.8 PgC y^{-1} ‰ and 66 PgC y^{-1} ‰ for land and ocean derived in this study (Table 4), respectively,

577 we also calculated the land and ocean sinks to be 2.90 and 2.36 PgC y^{-1}, respectively. The ratio

578 between land and ocean sinks is 1.23, which is close to the value of 1.07 derived from the joint

579 inversion system, indicating that the joint inversion can effectively perform double deconvolution.

580 Our joint inversion system differs from previous double deconvolution systems (*Siegenthaler and*

581 *Oeschger,* 1987*; Keeling et al.,* 1989a; *Francey et al*., 1995; *Randerson et al*., 2002) in the following

582 ways: (1) the estimation of CO_2 fluxes for the land and ocean is additionally constrained by the prior

583 fluxes for the land and ocean rather than entirely dependent on measured CO_2 concentration and

584 $^{13}CO_2$ composition; and (2) the spatio-temporal variations in all parameters associated with isotopic

585 discrimination and disequilibrium are considered in the estimation of the CO_2 flux using a

586 mechanistic biospheric model rather than global average values or simple models based on covariates.

587 These differences in methodology as well as the differences in the mean disequilibrium fluxes may

588 explain why the ocean and land sinks from the joint inversion system differ from the various double

589 deconvolution results.

590   The impacts of $^{13}CO_2$ data on the joint inversion can also be evaluated from the view point of

591 global $^{13}CO_2$ mass budget. Table 5 shows the budgets and its components for the prior, double

592 deconvolution, CO_2-only inversion and joint inversion cases. In these cases, the isofluxes due to

593 fossil fuel emission, land and ocean disequilibrium, and atmospheric storage change are the same,

594 and only those due to discrimination over land and ocean are adjusted. The prior case shows a global

595 imbalance of -5.0 PgC y^{-1} ‰, indicating that either the prior land or ocean fluxes or both are

596 inconsistent with $^{13}CO_2$ measurements. Through double deconvolution, this imbalance is greatly

597 reduced to 0.8 PgC y^{-1} ‰, mostly by an increase in the discrimination flux over land because of its

598 large discrimination rate. The CO_2-only inversion increases the land discrimination flux while

599 decreasing the ocean discrimination flux, resulting in no improvement in the global isotopic balance.

600 The joint inversion optimized both ocean and land fluxes in the direction consistent with $^{13}CO_2$

601 measurements, reducing the imbalance considerably to 1.8 PgC y^{-1} ‰. These cases illustrate clearly

602 that the global isotopic mass balance is very sensitive to the partition between ocean and land fluxes

603 because of the large difference in the discrimination rate between land and ocean. In this analysis, the

604 disequilibrium fluxes are not adjusted, but the influences of the uncertainties in these fluxes on the

605 inversion results are analyzed in Section 3.2.4.

606   Existing estimates for the ocean sink for anthropogenic CO_2 in 2000's varies from 1.94 to 2.6

607 Pg C y^{-1} (*Wanninkhof et al*., 2013; *Landchuster et al.*, 2014; *Majkut et al.*, 2014; *DeVries*, 2014). The

608 average ocean sink for the 2002-2004 period summarized by the Global Carbon Project (GCP) (*Le*

609 *Quéré et al*., 2013) is 2.4 Pg C y^{-1}, while the land sink in the same period is 2.7 Pg C y^{-1} as the

610 residual of the global carbon budget after including the emission due to land use change as a source

611 of carbon. Although the prior estimates of these sinks in our inversions are similar to these values,

612 our CO_2-only inversion considerably increases the land sink and decreases the ocean sink. The

613 addition of $^{13}CO_2$ measurements to the inversion significantly decreases the land sink and increases

614 the ocean sink, pulling the inversion results in the direction to agree with these existing estimates

615 (Figure 7). This may indicate that the use of $^{13}CO_2$ measurements in the joint inversion has improved

616 the CO_2 estimation. In this comparison, we have not considered the unknown small amount (0.1-0.3

617 Pg C y^{-1}) of lateral carbon transport in rivers from land to ocean. This amount is included in some of

618 the estimates of the ocean sink used by GCP, and therefore should be subtracted from the ocean sink

619 and added to the land sink by GCP in order to compare with our atmospheric inversion results.

620 3.2.2 Influence of $^{13}CO_2$ constraint on the spatial distribution of the inverted carbon flux

621   The $^{13}CO_2$ constraint not only modified the partition between ocean and land fluxes but also

622 their spatial distribution patterns. Figure 8 shows the result of the CO_2-only inversion (i.e. without

623 the $^{13}CO_2$ constraint), as the net carbon flux over land and ocean averaged for the period of 2002-

624 2004. Figure 9 shows the difference between inversions with and without the $^{13}CO_2$ constraint, i.e.

625 the result of $CO_2+^{13}CO_2$ inversion minus that of CO_2–only inversion. The general patterns of the

626   inverted carbon flux are similar between these two inversions because these inversions depend

627   primarily on the CO_2 concentration, the prior flux, the error matrixes of the prior flux, and

628   concentration observations. However, there are several large or notable differences: (1) The Amazon

629   region (Region 31) is changed from a carbon source to a sink (Figure 10. Note: a reduction in sources

630   is shown as a negative value); (2) the carbon sink in the tropical Asia (Region 37) is noticeably

631   reduced (by about 10-20 gC m^{-2}y^{-1} from a sink magnitude of about 80-100 gC m^{-2}y^{-1}); (3) The sink in

632   Asia (Region 36) decreases pronouncedly by about 10-20 gC m^{-2}y^{-1}, while the sinks in Russia

633   (Region 35) and Europe (Region 39) are also reduced by some extents (about 5-20 gC m^{-2}y^{-1}); (4)

634   most small regions in the southern part of North America show increases in sinks, but those in the

635   northern part (Canada and Alaska) show increases in sources (see also Figure 11). The overall sink

636   in North America decreases from 0.67 to 0.54 Pg C y^{-1} (Figure 10); and (5) most ocean regions at

637   mid-latitudes have small gains in sink.

638   It is of particular importance to note that the $^{13}CO_2$ constraint changed the Amazon region

639   from a carbon source of 0.43 ± 0.46 Pg C y^{-1} to a carbon sink of 0.08 ± 0.38 Pg C y^{-1} with a notable

640   reduction in the posterior uncertainty, which is higher than uncertainty reductions in most other

641   regions (Figure 10). This change is likely caused by the relatively large addition of information from

642     $^{13}CO_2$ in this tropical region where CO_2 observations are sparse, causing large uncertainties in the

643   inverted flux in this region in the CO_2-only inversion. *Potter et al.* (2009) simulated the net

644   ecosystem productivity (NEP) of the Amazon region using the CASA model driven by remote

645   sensing inputs and found that the NEP for the region was slightly negative (-0.07 Pg C y^{-1}) over the

646   2000-2004 period. *Davidson et al.* (2012) summarized from various inventory-based studies that

647   mature forests in the region was accumulating carbon at a rate of 0.29-0.57 Pg C y^{-1} over the decade

648   before 2005, meaning that NEP is positive. Since the fire emission is estimated to be 0.50 Pg C y^{-1}

649 (*Richey et al.,* 2002), the Amazon region would be either net source of carbon or about carbon

650 neutral. Since spatially explicit fire emission is considered together with fossil fuel emission as a

651 source in our study, the inverted carbon flux corresponds to –NEP, and therefore the result from our

652 joint inversion is in broad agreement with Potter's and Davidson's results. Without the $^{13}CO_2$

653 constraint, our inversion result shows an unreasonably large source of carbon in the Amazon region.

654   3.2.3 Influence of the spatial distribution of photosynthetic discrimation on the inverted carbon

655 flux

656   The joint inversion results shown in Figures 9 to 11 are from Case I with the best estimates of

657 the ^{13}C discrimination and disequilibrium fluxes and therefore represent a baseline study to which

658 other cases are compared for the purpose of investigating the importance of accurate consideration of

659 the spatial distributions of isotopic discrimination and disequilibrium over land and ocean. Case II is

660 designed to investigate the importance of considering the spatial distribution of the photosynthetic

661 isotopic discrimination over land for inverting the CO_2 flux by fixing the discrimination at a constant

662 over land. Figure 12a shows the spatial distribution of the difference in the total isotopic

663 discrimination, i.e. $D_j = \varepsilon_{lph,j}$, among 39 land regions between Case I and Case II, calculated as Case

664 I minus Case II. Regions with positive differences in D_j are shown with positive differences in the

665 inverted CO_2 flux (Figure 12b), meaning larger sinks (negative values) in Case II, and vice versa.

666 This is because a smaller discrimination rate (smaller than -14.1‰) means a larger CO_2 flux from the

667 atmosphere to the surface (more negative value) for the same change in $^{13}CO_2$ concentration in the

668 atmosphere. Under the same condition, a larger discrimination induces a smaller sink (less negative).

669 The absolute regional differences between Case I and Case II are considerable (Figure 12b), e.g. up

670 to 18 g C m^{-2}y^{-1}, showing increases in sinks in Africa, Asia and Australia and decreases in sinks in

671   Amazon, Europe, Russia and most of the small regions in North America. However, the total global

672   sink values of Case II after ignoring the spatial distribution of the disequilibrium rate over land

673   change very little from those of Case I (Table 3): from 2.53±0.93 to 2.49±0.95 Pg C y^{-1} for land and

674   from 2.36±0.49 to 2.35±0.48 Pg C y^{-1} for ocean. This is because the global mean discrimination rates

675   are the same between these two cases.

676   3.2.4 Influence of the uncertainties in disequilibrium fluxes on the inverted carbon flux

677   The average disequilibrium coefficients and fluxes for land and ocean derived in this study are

678   comparable to published results (Table 4), although the estimates of the disequilibrium flux over

679   ocean in previous studies vary in a large range. The uncertainty in the estimated land and ocean

680   disequilibrium fluxes mainly arises from two sources: the estimated disequilibrium coefficient and

681   one-way CO_2 flux from the surface. Mathematically, the total uncertainty in the disequilibrium flux,

682   denoted as $\Delta(\delta{\cdot}F)$, equals $\sqrt{(\Delta\delta \cdot F)^2 + (\delta \cdot \Delta F)^2}$. For land, the first source depends on the modeled

683   mean soil carbon age by BEPS, which is estimated to be ±5 years, causing an error in the

684   disequilibrium coefficient to be ±0.11‰ based on the slope of δ_a against time at about 1979 (the

685   flux-weighted global mean soil carbon age is 24 years). The second source is estimated to be 9.5 PgC

686   y^{-1} in NPP, which is taken as 45% of the error in GPP, i.e. 21 PgC y^{-1} (*Chen et al.,* 2012). With

687   NPP=59.4 PgC y^{-1} and the mean disequilibrium efficient of 0.49‰, the uncertainty in the estimated

688   land disequilibrium flux is therefore $\sqrt{(0.11\times59.4)^2 + (0.49\times9.5)^2} = 8.0$ PgC y^{-1} ‰. For ocean, the

689   error in the modeled disequilibrium coefficient is mostly caused by sea surface temperature (SST), if

690   the coefficients in the equation developed by *Ciais et al.* (1995b) are assumed to be accurate. With an

691   error of 1.0K in SST, the error in the calculated global average disequilibrium coefficient is ±0.12‰.

692   The error in one-way the ocean flux is difficult to estimate, but we use the value of 10 PgC y^{-1}

693   inferred from the global isotopic budget uncertainty by *Alden* et al. (2010). Their inferred range of

694   the ocean disequilibrium flux is from 92.3 to100.2 PgC y^{-1} ‰, and we use our disequilibrium

695   coefficient of 0.78‰ to calculate this one-way flux uncertainty. Based on the OPA-PISCES-T model,

696   the one-way flux from ocean to atmosphere is 84.6 PgC y^{-1}, and the uncertainty in the estimated

697   ocean disequilibrium flux is therefore $\sqrt{(0.12 \times 84.6)^2 + (0.78 \times 10)^2} = 12.7$ PgC y^{-1} ‰.

698   Case III, Case IV and Case V are conducted to investigate the relative importance of the

699   disequilibrium fluxes over land and ocean (Table 3) in the CO2 flux inversion. In Case III, where the

700   disequilibrium over land is ignored while other settings remain the same as Case I, the land sink

701   increases by 1.05 PgC y^{-1}, while the ocean sink decreases by 0.08 PgC y^{-1} in comparison with Case I.

702   When the disequilibrium over ocean is ignored instead (Case IV), the land sink increases by 0.13

703   PgC y^{-1}, while the ocean sink increases by 2.08 PgC y^{-1}, in comparison with Case I. When the

704   disequilibria over both land and ocean are ignored, the land sink increases by 1.18 PgC y^{-1}, while the

705   ocean sink increases by 1.96 PgC y^{-1}, in comparison with Case I. Results from these case studies

706   suggest that in the joint inversion using both CO_2 and $^{13}CO_2$ measurements, the inverted CO_2 flux

707   can be significantly influenced by the disequilibrium fluxes of land and ocean. The carbon sinks over

708   land and ocean increase when these disequilibrium fluxes are ignored because the photosynthetic and

709   diffusive sources of $^{13}CO_2$ have to increase to make up for the shortfall due to ignoring the

710   disequilibrium sources. These pronounced influences of the disequilibrium fluxes on the CO_2 sink

711   inversion suggest that $^{13}CO_2$ data contain strong signals for the global carbon cycle. In the joint

712   inversion, these data can have the power to distort the global CO_2 mass balance if the $^{13}CO_2$ mass

713   budget (Eq. 8) is not properly simulated. The influence of $^{13}CO_2$ on the joint inversion depends only

714   weakly on the estimated uncertainty in the $^{13}CO_2$ data. We found that if the uncertainty is reduced by

715 half, the sum of the land and ocean sink deviates from the CO_2-only case by 2-6% for all scenarios,

716 suggesting that the mean disequilibrium fluxes play the dominant roles in the joint inversion.

717   The impacts of these disequilibrium fluxes on the inverted CO_2 flux determined in Case III,

718 Case IV and Case V are similar to previous results using the double deconvolution technique (*Tans et*

719 *al.,* 1993; *Ciais et al.,* 1995b*; Randerson et al.,* 2002). However, the influences of these

720 disequilibrium fluxes on the joint inversion could possibly be compromised due to the small number

721 of ^{13}C observation sites relative to the number of CO_2 observation sites used in the joint inversion.

722 The number of linear equations for CO_2 concentration in our joint inversion system (Eq. 6) greatly

723 exceeds the number for ^{13}C composition, with a potential of dampening the impact of ^{13}C data on the

724 inverted results. To investigate the possibility of this dampening effect, we conducted a set of

725 inversions using ^{13}C data alone (Table 6) and found that the impacts of the disequilibrium fluxes on

726 the inversion results are similar to those of the joint inversion. In Case V shown in Table 6, for

727 example, ignoring the disequilibrium fluxes causes the land sink to increase by 1.06 PgC y^{-1} and

728 ocean sink to increase by 2.37 PgC y^{-1}, resulting in a total increase of 3.43 PgC y^{-1}, which is similar

729 to the total difference of 3.14 PgC y^{-1} produced by the joint inversion. These similar results suggest

730 that ^{13}C data used in the way described by Eqs. 6-8 have played the expected role in the joint

731 inversion. By comparing results shown in Tables 3 and 6, it is also encouraging to see that inversions

732 using ^{13}C data alone can produce reasonable results for the CO_2 flux, although we believe that the

733 joint inversion results shown in Table 3 are more reliable. Our finding on the usefulness of the small

734 $^{13}CO_2$ dataset somewhat confirms the claim of Enting et al. (1993 and 1995) that the temporal trend

735 in $^{13}CO_2$ concentration is the major signal constraining the partition between ocean and land sinks.

736   According to the difference of the inverted flux between Case III to Case I, the uncertainty of

737 8.0 PgC y^{-1} ‰ in the land disequilibrium flux would cause an uncertainty of 0.47 PgC y^{-1} in the land

738   flux. According to the comparison between Case IV to Case I, the uncertainty of 12.7 PgC y^{-1} ‰ in

739   the ocean disequilibrium flux would cause an uncertainty of 0.54 PgC y^{-1} in the ocean flux. These

740   uncertainties in the land and ocean fluxes are 17% and 24% of the jointly inverted fluxes for land and

741   ocean (Case I in Table 3), respectively. The impact of the uncertainty in the disequilibrium flux over

742   land is only slightly smaller than the posterior uncertainty of the inverted land flux, but the impact

743   over ocean is larger than the posterior uncertainty.

744   **Discussion**

745   After the CO_2 fluxes are optimized through the inversions, the posterior CO_2 concentration at

746   all stations in each month can be calculated from Eq. 2, and similarly the posterior $^{13}CO_2$

747   composition can also be calculated from Eq. 10 by replacing the prior discrimination fluxes with

748   posterior discrimination fluxes. One way to evaluate the effectiveness of the joint inversion is to

749   examine the improvement in the posterior CO_2 and $^{13}CO_2$ concentrations against measurements.

750   Figure 13 shows concentrations for 10 randomly selected stations from different regions, which are

751   indicated in Figure 1. The CO_2 and $^{13}CO_2$ concentrations produced using the prior fluxes

752   considerably deviate from observations at all stations. The posterior CO_2 concentration from the

753   CO_2-only inversion shows great improvements over the prior concentration in comparison with

754   observations. The posterior CO_2 concentration from the joint inversion does not differ significantly

755   from that of the CO_2-only inversion. At some stations the joint inversion produces slightly lower root

756   mean square differences (RMSD) against observations, but in some stations the opposite is true, as

757   indicated by the RMSD values shown in the header of each plot. It is expected that in some stations,

758   the posterior CO_2 concentration in the joint inversion can be slightly worsened because of the

759   influence of $^{13}CO_2$. The posterior $^{13}CO_2$ concentration is pronouncedly improved over the prior in

760   comparison with observations and almost mimics the observed magnitudes and temporal variations,

761   indicating that the joint inversion system can forcefully adjust CO_2 fluxes to match with $^{13}CO_2$

762   observation through the prescribed discrimination rates. The posterior CO_2 concentrations for either

763   CO_2-only or joint inversion show larger seasonal amplitudes than observations at northern

764   hemisphere stations, although the means are about the same as observations. This suggests that both

765   carbon uptake during the growing season and ecosystem respiration in the non-growing season might

766   have been overestimated, even though the annual net carbon flux may be unbiased. Further work is

767   needed to constrain the large photosynthetic and respiratory fluxes separately rather than the net flux

768   only.

769   In order to provide a comprehensive evaluation, the posterior CO_2 and $^{13}CO_2$ concentrations at

770   all stations are shown in Figures 14 and 15 against observations. In Figure 14, we see pronounced

771   improvements in the posterior concentrations from both the CO_2-only and joint inversions over the

772   prior case. However, the improvements of these two inversions are similar (the joint inversion has a

773   smaller intercept and a slope closer to one, but the CO_2-only inversion has a slightly larger r^2 value).

774   This is in agreement with the cases shown for the individual stations: some stations are improved and

775   some worsened by the use of $^{13}CO_2$ data, manifesting the force of this additional data on the

776   inversion. In Figure 15, the posterior $^{13}CO_2$ concentration from the joint inversion is shown to be

777   greatly improved from the prior case. In the joint inversion, the increase of the posterior land and

778   ocean sinks over the prior sinks that remove CO_2 from the atmosphere logically corrects for the

779   positive bias in the CO_2 concentration produced using the prior fluxes (Figure 14a). The posterior

780   concentration correlation with observation is stronger for $^{13}CO_2$ than for CO_2, indicating that

781   isofluxes are effectively optimized in the joint inversion according to $^{13}CO_2$ data. However, some

782   points in Figure 15b scatter greatly from the 1:1 line, and these points are mostly likely the missing

783   data filled with the reference data (Section 2.4). As other error sources cannot be excluded, these data

784   are retained in our inversion.

785   After adding $^{13}CO_2$ data to the inversion system, the uncertainty in the inverted CO_2 flux

786   changed from 0.84 to 0.93 PgC y^{-1} for land and from 0.40 to 0.49 PgC y^{-1} for ocean (Table 3,

787   difference between the CO_2-only case and Case I), i.e. 11% and 23% changes in uncertainty for land

788   and ocean, respectively. In the joint inversion, the relative error in$^{13}CO_2$ measurements is similar to

789   that in CO_2 measurement and the uncertainty in the prior $^{13}CO_2$ flux estimation is not required, and

790   therefore the posterior uncertainty in the inverted CO_2 flux does not directly take into account of the

791   error in the prior $^{13}CO_2$ flux estimation. However, through the use of modeled photosynthetic

792   discrimination and the disequilibrium fluxes over land and ocean, the prior $^{13}CO_2$ flux estimation has

793   influence on the inversion results. Errors in modeling the spatial and temporal variations of the $^{13}CO_2$

794   flux stem from many sources including errors in modeling the discrimination, which is affected by

795   the fractionation of the $^{13}CO_2$ flow through leaf boundary layer, stomata, mesophyll, etc., and the

796   disequilibrium, which depends on the sizes of 9 soil carbon pools and their ages. Although the ocean

797    $^{13}CO_2$ discrimination is small, its disequilibrium has a strong latitudinal gradient, which is

798   approximately calculated using the mean monthly temperature. The error in the calculated ocean

799   disequilibrium coefficient is estimated to be $\pm$ 1.2‰ for the monthly values at a given location and $\pm$

800   0.12‰ for the global annual total. Because of these errors, we estimate that the relative uncertainty in

801   the prior $^{13}CO_2$ fluxes is similar to that of the prior CO_2 flux over both land and ocean.

802

803   **4. Conclusion**

804   The usefulness of atmospheric $^{13}CO_2$ measurements at 73 stations for global carbon cycle

805   estimation is explored through their use as an additional constraint on an atmospheric inversion of

806   the surface carbon flux using CO_2 observations. The following conclusions are drawn from this

807   study:

808   1. This ^{13}C constraint on the joint inversion considerably alters the partition between land and

809   ocean sinks obtained from CO_2-only inversion, decreasing the land sink from 3.40±0.84 to

810   2.53±0.93 Pg C y^{-1}, while increasing the ocean sink from 1.48±0.40 to 2.36±0.49 Pg C y^{-1} for

811   the 2002-2004 period. Over land, this alteration induces the largest sink increases in the

812   Amazon region and largest source increases in southern Africa and Asia, where CO_2

813   observations are sparse and therefore the additional signal from $^{13}CO_2$ data becomes most

814   important. Over ocean, sink increases are found broadly at middle and high latitudes in both

815   hemispheres.

816   2. The spatial distribution of the $^{13}CO_2$ discrimination rate over land has considerable impacts

817   on the spatial distribution of the inverted CO_2 sink over land (up to 15% in some regions),

818   suggesting that reliable models for simulating the spatial distribution of the ^{13}C discrimination

819   rate over land are needed for effective use of $^{13}CO_2$ data for global carbon cycle inversion.

820   **3.** The joint inversion is sensitive to the $^{13}CO_2$ disequilibrium fluxes over both land and ocean.

821   Ignoring these fluxes in the joint inversion causes the inverted total land and ocean sink to

822   increase by 1.18 and 1.96 PgC y^{-1}, respectively. The uncertainty in our disequilibrium flux

823   calculation is estimated to be 8.0 PgC y^{-1} ‰ and 12.7 Pg C y^{-1} ‰ for land and ocean,

824   respectively, inducing an uncertainty in the inverted flux of 0.47 Pg C y^{-1} for land and 0.54 Pg

825   C y^{-1} for ocean.

826   **Acknowledgement**

827   We greatly appreciate the GlobalView dataset that is available from the NOAA Climate

828   Monitoring and Diagnostics Laboratory. NCEP/DOE 2 Reanalysis data are provided by the

829   NOAA/OAR/ESRL PSD, Boulder, Colorado, USA, from their Web site at

830   http://www.esrl.noaa.gov/psd/. This research was support by a grant (2010CB950704) from the

831   Global Change Key Program of the Chinese Ministry of Science and Technology and a grant (GR-

832   646) from the former Canadian Foundation for Climate and Atmospheric Sciences. Drs. Misa

833   Ishizawa, Douglas Chan and Kaz Higuchi of Environment Canada (EC) provided useful suggestions

834   and technical assistance at the beginning of the project, and Jonathan Fung assisted in the CO_2-only

835   inversion during his M.Sc. studies. We are also indebted to Drs. Pieter Tans of NOAA and Lin

836   Huang of EC for their guidance in the development and validation of the isotope module in BEPS in

837   the early years. Dr. Peter Rayner was a critical and constructive reviewer of several versions of this

838   paper and provided high-level intellectual inputs to this study which are greatly appreciated.

839   **4. References**

840   Alden, C., J. B. Miller, and J. W. C. White (2010), Can bottom-up ocean CO2 fluxes can be
841   reconciled with atmospheric 13C observations?, *Tellus B*, 62B, 369-388.
842
843   Andres R.J., G. Marland, T. Boden T., and S. Bischof (2000), Carbon dioxide emissions from fossil
844   fuel consumption and cement manufacture, 1751-1991, and an estimate of their isotopic composition
845   and latitudinal distribution, in Wigley T.M.L., Schimel D.S. (eds.) *The Carbon Cycle*. Cambridge:
846   Cambridge University Press. 53-62.
847
848   Aumont, O., E. Maier-Reimer, S. Blain, and P. Monfray (2003), An ecosystem model of the global
849   ocean including Fe, Si, P colimitations, *Global Biogeochem. Cycles*, *17*(2), 1060.
850
851   Baker, D. F., R. M. Law, K. R. Gurney, P. Rayner, P. Peylin, A. D. Denning, P. Bousquet, L.
852   Bruhwiler, Y. H. Chen, P. Ciais, I. Y. Fung, M. Heimann, J. John, T. Maki, S. Maksyutov, K.
853   Masarie, M. Prather, B. Pak, S. Taguchi, and Z. Zhu (2006), TransCom 3 inversion intercomparison:
854   Impact of transport model errors on the interannual variability of regional
855   CO2 fluxes, 1988–2003, Global Biogeochem. Cy., 20, GB1002, doi:10.1029/2004GB002439.

856

857 Ball, J. T. (1988), An analysis of stomatal conductance, Ph.D. thesis, 89 pp., Stanford Univ.,
858 Stanford, Calif.

859 Beer, C., M. Reichstein, E. Tomelleri, P. Ciais, M. Jung, N. Carvalhais, C. Rodenbeck, M.A. Arain,
860 D. Baldocchi, G.B. Bonan, A. Bondeau, A. Cescatti, G. Lasslop, A. Lindroth, M. Lomas, S.
861 Luyssaert, H. Margolis, K.W. Oleson, O. Roupsard, E. Veenendaal, N. Viovy, C. Williams, F.I.
862 Woodward, and D. Papale (2010), Terrestrial Gross Carbon Dioxide Uptake: Global Distribution and
863 Covariation with Climate, *Science* 329:834-838.

864 Buitenhuis, E., C. Le Quéré, O. Aumont, G. Beaugrand, A. Bunker, A. Hirst, T. Ikeda, T. O'Brien, S.
865 Piontkovski, and D. Straile (2006), Biogeochemical fluxes through mesozooplankton, *Global
866 Biogeochem. Cycles*, *20*(2), GB2003.

867 Canadell, J. G., C. Le Quéré, M. R. Raupach, C. B. Field, E. T. Buitenhuis, P. Ciais, T. J. Conway,
868 N. P. Gillett, R. A. Houghton, and G. Marland (2007), Contributions to accelerating atmospheric CO_2
869 growth from economic activity, carbon intensity, and efficiency of natural sinks, *Proceedings of the
870 National Academy of Sciences*, *104*(47), 18866-18870.
871

872 Chen, B., J. M. Chen, P. Tabs and L. Huang (2006), Simulating dynamics of $^{13}CO_2$ in the planetary
873 boundary layer over a boreal forest region: An approach to estimate carbon isotope rectification.
874 *Tellus 58B*, 537-549.
875

876 Chen, B., and J. M. Chen, 2007. InterannualTemporal variation in carbon isotope discrimination in
877 response to meteorological and physiological driving factors in a boreal forest ecosystem, *Plant, Cell
878 and Environment,* 30: doi: 10.1111/j.1365-3040.2007.01707.

879 Chen, J. M., J. Liu, J. Cihlar, and M. L. Goulden (1999), Daily canopy photosynthesis model through
880 temporal and spatial scaling for remote sensing applications, *Ecological Modelling*, *124*(2-3), 99-119.
881

882 Chen, J. M., W. Ju, J. Cihlar, D. Price, J. Liu, W. Chen, J. Pan, T. A. Black, and A. Barr (2003),
883 Spatial distribution of carbon sources and sinks in Canada's forests based on remote sensing, *Tellus B*.
884 55(2): 622-642.

885 Chen, J. M., C. H. Menges, and S. G. Leblanc (2005), Global derivation of the vegetation clumping
886 index from multi-angular satellite data, *Remote Sensing of Environment,* 97: 447-457.

887 Chen, J. M., G. Mo, J. Pisek, J. Liu, F. Deng, M. Ishizawa, and D. Chan (2012), Effects of foliage
888 clumping on the estimation of global terrestrial gross primary productivity, *Global Biogeochem.
889 Cycles*, 26, GB1019, doi:10.1029/2010GB003996.

890 Chen, J. M., J. Fung, G. Mo, F. Deng, and T. West (2015), Atmospheric inversion of the global
891 surface carbon flux with consideration of the spatial distribution of US crop production and
892 consumption. *Biogeosciences,* 12, 323-343.
893

894 Ciais, P., P. P. Tans, M. Trolier, J.W. C. White, and R. J. Francey (1995a). A large northern-
895 hemisphere terrestrial CO2 sink indicated by the 13C/12C ratio of atmospheric CO2. *Science,* 269,
896 1098-1102.

898 Ciais, P., P. P. Tans, J. W. C. White, M. Trolier, R. J. Francey, J. A. Berry, D. R. Randall, P. J.
899 Sellers, J. G. Collatz, and D. S. Schimel (1995b), Partitioning of ocean and land uptake of CO_2 as
900 inferred by $\delta^{13}C$ measurements from the NOAA Climate Monitoring and Diagnostics Laboratory
901 Global Air Sampling Network, *J. Geophys. Res.*, 100(D3), 5051–5070, doi:10.1029/94JD02847.

903 Davidson, E. A., A. C. de Araujo, P. Artaxo et al., (2012), The Amazon basin in transition. *Nature,*
904 481, 321-328.

906 Deng, F., J. M. Chen, M. Ishizawa, C.-W. Yuen, G. Mo, K. A. Z. Higuchi, D. Chan, and S.
907 Maksyutov (2007), Global monthly CO_2 flux inversion with a focus over North America, *Tellus B*,
908 *59*(2), 179-190.

910 Deng, F., J. M. Chen, S. Plummer, M. Chen, and J. Pisek (2006), Algorithm for global leaf area
911 index retrieval using satellite imagery, *IEEE Transactions on Geoscience and Remote Sensing*, *44*(8),
912 2219-2229.

914 Deng, F., and J. M. Chen (2011), Recent global CO_2 flux inferred from atmospheric CO_2
915 observations and its regional analysis. *Biogeosciences,* 8: 3263–3281.
916 DeVries, T. (2014), The oceanic anthropogenic CO2 sink: Storage, air-sea fluxes, and transports over
917 the industrial era, *Global Biogeochem. Cycles*, *28*, 631–647, doi:10.1002/2013GB004739.

919 Enting, I.G., C.M. Trudinger, R.J. Francey and H. Granek (1993), Synthesis inversion of atmospheric
920 CO_2 using the GISS tracer transport model, *Division of Atmospheric Research technical paper,*
921 No.29, CSIRO Australia.

923 Enting, I. G., C. M. Trudinger, and R. J. Francey (1995), A synthesis inversion of the concentration
924 and $\delta^{13}C$ of atmospheric CO_2. *Tellus B*, 47: 35–52.

926 Enting, I. G. (2002), *Inverse Problems in Atmospheric Constituents transport*, Cambridge University
927 Press.

929 Farquhar, G. D., S. von Caemmerer, and J. A. Berry (1980), A biochemical model of photosynthetic
930 CO_2 assimilation in leaves of C3 species, *Planta,* 149, 78–90, doi:10.1007/BF00386231.

932 Farquhar, G. D., and R. A. Richards (1984), Isotopic composition of plant carbon correlates with
933 water-use efficiency of wheat genotypes, *Aust., J. Plant. Physiol*., 11, 539–552.

934 Farquhar G.D., J. R. Ehleringer and K. T. Hubick (1989), Carbon isotope discrimination and
935 photosynthesis. *Annual Review of Plant Physiology and Plant Molecular Biology.* 40:503–537.

936 Francey, R. J., P. P. Tans, C. E. Allison, I. G. Enting, J. W. C. White, and M. Trolier (1995),
937 Changes in oceanic and terrestrial carbon uptake since 1982. *Nature*, 373, 326–330.
938
939 Francey R. J., C. E. Allison, D. M. Etheridge, C. M. Trudinger, I. G. Enting, M. Leuenberger, R. L.
940 Langenfelds, E. Michel, L. P. Steele (1999), A 1000-year high precision record of $\delta^{13}C$ in
941 atmospheric CO_2, *Tellus B*, 51(2), 170–193.
942
943 Fung, I.Y., C. B. Field, J. A. Berry, M. V. Thompson, J. T. Randerson, C. M. Malmström, P. M.
944 Vitousek, G. James Collatz, P. J. Sellers, D. A. Randall, A. S. Denning, F. Badeck (1997), Carbon-
945 13 exchanges between the atmosphere and biosphere, *Global Biogeochemical Cycles,* 11: 507-533.

946 Garrigues S., R. Lacaze, F. Baret, J.T. Morisette, M. Weiss, J.E. Nickeson, R. Fernandes, S.
947 Plummer, N.V. Shabanov, R.B. Myneni, Y. Knyazikhin, W. Yang (2008), Validation and
948 intercomparison of global Leaf Area Index products derived from remote sensing data, *J. Geophys.
949 Res*., 113, G02028:doi:10.1029/2007JG000635.

950 GLOBALVIEW-CO2C13: Cooperative Atmospheric Data Integration Project - $\delta^{13}C$ of Carbon
951 Dioxide. CD-ROM, NOAA ESRL, Boulder, Colorado [Also available on Internet via anonymous
952 FTP to ftp.cmdl.noaa.gov, Path: ccg/co2c13/GLOBALVIEW], 2009.

953 Govind, A., and J. M. Chen (2011), Spatially distributed modeling of the long-term carbon balance
954 of a boreal landscape. *Ecological Modeling,* doi:10.1016/j.ecolmodel.2011.04.007.

955 Gurney, K. R., R. M. Law, A. S. Denning, P. J. Rayner, D. Baker, P. Bousquet, L. Bruhwiler, Y. H.
956 Chen, P. Ciais, S.M. Fan, I. Y. Fung, Manuel Gloor, Martin Heimann, K Higuchi, J. John, T Maki, S.
957 Maksyutov, K. Masarie, P. Peylin, M. Prather, B. C. Pak, J. T. Randerson, J. L. Sarmiento, S.
958 Taguchi, T Takahashi, C. W. Yuen (2002), Towards robust regional estimates of CO_2 sources and
959 sinks using atmospheric transport models, *Nature*, *415*(6872), 626-630.

960 Gurney, K. R., K. R. Gurney, R. M. Law, A. S. Denning, P. J. Rayner, D. Baker, P. Bousquet, L.
961 Bruhwiler, Y. H. Chen, P. Ciais, S.M. Fan, I. Y. Fung, M. Gloor, M. Heimann, K. Higuchi, J. John, E.
962 Kowalczyk, T. Maki, S. Maksyutov, P. Peylin, M. Prather, B. C. Pak, J. L. Sarmiento, S. Taguchi, T.
963 Takahashi, C. W. Yuen (2003), TransCom3 CO_2 inversion intercomparison: 1. Annual mean control
964 results and sensitivity to transport and prior flux information, *Tellus B*, *55*(2), 555-579.
965
966 Harley, P. C., F. Loreto, G. Di Marco, and T. D. Sharkey (1992), Theoretical Considerations when
967 Estimating the Mesophyll Conductance to CO_2 Flux by Analysis of the Response of Photosynthesis
968 to CO_2, *Plant Physiol.* 98:1429–1436.

969 Houghton, R.A. (2007), Balancing the global carbon budget, *Annual Review of Earth and Planetary
970 Sciences* 35:313-347.
971
972 Ise, T., C. M. Litton, C. P. Giardina, and A. Ito (2010), Comparison of modeling approaches for
973 carbon partitioning: impact on estimates of global net primary production and equilibrium biomass of

974   woody vegetation from MODIS GPP. *Journal of Geophysical Research*, Vol., 115, G04025,
975   doi:10.1029/2010JG001326.

976   Jacobson, A., S. Fletcher, N. Gruber, J. Sarmiento, and M. Gloor (2007), A joint atmosphere-ocean
977   inversion for surface fluxes of carbon dioxide: 2. Regional results, *Global Biogeochem. Cycles*, *21*(1),
978   GB1020, doi:10.1029/2006GB002703.

980   Ju, W., and J. M. Chen (2005), Distribution of soil carbon stocks in Canada's forests and wetland
981   simulated based on drainage class, topography and remote sensing. *Hydrological Processes*, 19:77-
982   94.

984   Kalnay, E., M. Kanamitsu, R. Kistler, W. Collins, D. Deaven, L. Gandin, M. Iredell, S. Saha, G.
985   White, J. Woollen, Y. Zhu, A. Leetmaa, B. Reynolds, M. Chelliah, W. Ebisuzaki, W. Higgins, J.
986   Janowiak, K. C. Mo, C. Ropelewski, J. Wang, R. Jenne, and D. Joseph (1996), The NCEP/NCAR
987   40-year reanalysis project, *Bull. Amer. Meteor. Soc.*, *77*, 437-471.

989   Kanamitsu, M., W. Ebisuzaki, J. Woollen, S-K Yang, J. J. Hnilo, M. Fiorino, and G. L. Potter.
990   (2002), NCEP-DEO AMIP-II Reanalysis (R-2), *Bulletin of the American Meterological Society,*
991   1631-1643.

993   Keeling, C. D., R. B. Bacastow, A. F. Carter, S. C. Piper, T. P. Whorf, and co-authors (1989a). A
994   three-dimensional model of atmospheric CO2 transport based on observed winds: 1. analysis of
995   observational data. In: Aspects of climate variability in the Pacific and Western Americas (ed.
996   Peterson, D. H.). American Geophysical Union, Washington, D.C., 165-236.

998   Keeling, C. D., S. C. Piper, and M. Heimann (1989b). A three-dimensional model of atmospheric
999   CO2 transport based on observed winds: 4. Mean annual gradients and interannual variations. In:
1000 Aspects of climate variability in the Pacific and Western Americas (ed. Peterson, D. H.). American
1001 Geophysical Union, Washington D.C., 305-363.

1003 Krol, M. C., J. Lelieveld, D. E. Oram, G. A. Sturrock, S. A. Penkett, C. A. M. Brenninkmeijer, V.
1004 Gros, J. Williams, and H. A. Scheeren (2003), Continuing emissions of methyl chloroform from
1005 Europe, *Nature*, *421*(6919), 131-135.

1006 Krol, M. C., S. Houweling, B. Bregman, M. van den Broek, A. Segers, P. van Velthoven, W. Peters,
1007 F. Dentener, and P. Bergamaschi (2005), The two-way nested global chemistry-transport zoom
1008 model TM5: algorithm and applications, *Atmos. Chem. Phys.*, *5*(2), 417-432.

1009 Landschützer, P., N. Gruber, D. C. E. Bakker, and U. Schuster, (2014), ecent variability of the
1010 global ocean carbon sink. *Global Biogeochemical. Cycles*, *28*, 927–949, doi:10.1002/2014GB004853.

1011 Le Quéré, C, Andres, R. J., Boden, T., Conway, T., Houghton, R. A., House, J. I., Marland, G.,
1012 Peters, G. P., van der Werf G. R., Ahlstrom, A., Andrew, R. M., Bopp, L., Canadell, J. G., Ciais, P.,
1013 Doney, S. C., Enright, C., Friedlingstein, P., Huntingford, C., Jain, A. K., Jourdain, C., Kato, E.,
1014 Keeling, R. F., Klein G. K., Levis, S., Levy, P., Lomas, M., Poulter, B., Raupach, M. R., Schwinger,

J., Sitch, S., Stocker, B. D., Viovy, N., Zaehle. S., and Zeng. N. (2013). The global carbon budget 1959–2011. *Earth Syst. Sci. Data* 5: 165–185, doi:10.5194/essd-5-165-2013.

Liu, J., J. M. Chen, J. Cihlar, and W. M. Park (1997), A process-based boreal ecosystem productivity simulator using remote sensing inputs, *Remote Sensing of Environment*, *62*(2), 158-175.

Madec, G., P. Delecluse, M. Imbard, and C. Lévy (1998), OPA 8.1 ocean general circulation model reference manual, *Notes du pôle de modélisation IPSL*, 91pp, http://www.lodyc.jussieu.fr/opa/.

Majkut, J. D., J. L. Sarmiento, and K. B. Rodgers (2014), A growing oceanic carbon uptake: results from an inversion study of surface pCO2 data. *Global Biogeochemical Cycles*, *28*, 335–351, doi:10.1002/2013GB004585.

Marland, G., T. A. Boden, and R. J. Andres (2009), Global, Regional, and National Fossil Fuel CO_2 Emissions. In Trends: A Compendium of Data on Global Change. Carbon Dioxide Information Analysis Center, Oak Ridge National Laboratory, U.S. Department of Energy, Oak Ridge, Tenn., U.S.A.

Masarie, K. A., and P. P. Tans (1995), Extension and integration of atmospheric carbon dioxide data into a globally consistent measurement record, *J. Geophys. Res*., 100(D6), 11593-11610.

Michalak, A. M., A. Hirsch, L. Bruhwiler, K. R. Gurney, W. Peters, and P. P. Tans (2005), Maximum likelihood estimation of covariance parameters for Bayesian atmospheric trace gas surface flux inversions, *J. Geophys. Res*., 110, D24107, doi:10.1029/2005JD005970.

Olivier, J. G. J., J. A. Van Aardenne, F. J. Dentener, V. Pagliari, L. N. Ganzeveld, and J. A. H. W. Peters (2005), Recent trends in global greenhouse gas emissions:regional trends 1970–2000 and spatial distributionof key sources in 2000, *Environmental Sciences*, *2*(2), 81 - 99.

Park, G. H., R. Wanninkhof, S. C. Doney, T. Takahashi, K. Lee, R. A. Feely, C. L. Sabine, J. Trinanes, and I. D. Lima, (2010), Variability of global net sea-air CO2 fluxes over the last three decades. Chemical and Physical Meteorology, 62, 352–368.

Patra, P. K., S. Maksyutov, M. Ishizawa, T. Nakazawa, T. Takahashi, and J. Ukita (2005), Interannual and decadal changes in the sea-air CO_2 flux from atmospheric CO_2 inverse modeling, *Global Biogeochem. Cycles*, *19*(4), GB4013.

Peters, W., J. B. Miller, J. Whitaker, S. A. Denning, A. Hirsch, M. Krol, D. Zupanski, L. Bruhwiler, and P. P. Tans (2005), An ensemble data assimilation system to estimate CO2 surface fluxes from atmospheric trace gas observations, J. Geophys. Res., 110, D24304, doi:10.1029/2005JD006157.

Peters, W. A. R. Jacobson, C. Sweeney, A. E. Andrews, T.J. Conway, K. Masarie, J. B. Miller, L. M. P. Bruhwiler, G. Petron, A. I. Hirsch, D. E. J. Worthy, G.R Werf, J. T. Randerson, P. O. Wennberg, M.C. Krol, P. P. Tans (2007), An atmospheric perspective on North American carbon dioxide exchange: CarbonTracker, *Proceedings of the National Academy of Sciences*, *104*(48), 18925-18930.

1058   Peylin, P., P. Bousquet, C. Le Quéré, S. Sitch, P. Friedlingstein, G. McKinley, N. Gruber, P. Rayner,
1059   and P. Ciais (2005), Multiple constraints on regional CO_2 flux variations over land and oceans.
1060   *Global Biogeochemical Cycles* 19: doi: 10.1029/2003GB002214.
1061

1062   Pickett-Heaps, C. A. (2007), Atmospheric CO_2 inversion cross-validation using non-surface CO_2
1063   data., *PhD dissertation*.

1064   Potter, C.S., J.T. Randerson, C.B., Field, P.A. Matson, P.M. Vitousek, H.A. Mooney, and S.A.
1065   Klooster (1993), Terrestrial ecosystem production: A process model based on global satellite and
1066   surface data, *Global Biogeochemical Cycles*,7 , 811-841.

1067   Potter, C., S. Klooster, A. Huete, V. Genovese, M. Bustamante, L. Guimaraes Ferreira, R. C. de
1068   Oliveira Jr., and R. Zepp, (2009), Terrestrial carbon sinks in the Brazilian Amazon and Cerrado
1069   region predicted from MODIS satellite data and ecosystem modeling. Biogeosciences, 6, 937–945.
1070

1071   Randerson, J. T., G. J. Collatz, J. E. Fessenden, A. D. Munoz, C. J. Still, J. A. Berry, I. Y. Fung, N.
1072   Suits, and A. S. Denning (2002), A possible global covariance between terrestrial gross primary
1073   production and ^{13}C discrimination: Consequences for the atmospheric ^{13}C budget and its response to
1074   ENSO, *Global Biogeochem. Cycles*, 16(4), 1136, doi:10.1029/2001GB001845
1075

1076   Randerson, J. T., G. R. van der Werf, L. Giglio, G. J. Collatz, and P. S. Kasibhatla (2007), Global
1077   Fire Emissions Database, Version 2 (GFEDv2.1). Data set. , *Available on-line [http://daac.ornl.gov/]*
1078   *from Oak Ridge National Laboratory Distributed Active Archive Center, Oak Ridge, Tennessee,*
1079   *U.S.A.*
1080

1081   Rayner, P. J, 2001. Atmospheric perspectives on the ocean carbon cycle. In E. D. Schulze, S. P.
1082   Harrison, M. Heimann, E. A. Holland, J. Lloyd, I. C. Prentice, and D. Schimel, editors, Global
1083   biogeochemical cycles in the climate system, pages 285–294. Academic Press, San Diego.

1084   Rayner, P. J., I. G. Enting, R. J. Francey, and R. L. Langenfelds (1999), Reconstructing the recent
1085   carbon cycle from atmospheric CO_2, $\delta^{13}C$ and O_2/N_2 observations, Tellus, Ser. B, 51, 213– 232.
1086

1087   Rayner, P. J., R. M. Law, C. E. Allison, R. J. Francey, C. M. Trudinger, and C. Pickett-Heaps (2008),
1088   Interannual variability of the global carbon cycle (1992–2005) inferred by inversion of atmospheric
1089 CO_2 and $\delta^{13}CO_2$ measurements, *Global Biogeochem. Cycles*, 22, GB3008,
1090   doi:10.1029/2007GB003068.

1091   Reynolds, R. W and T. M. Smith (1994), Improved global sea surface temperature analyses using
1092   optimum interpolation. *J. Climate*, 7, 929–948.

1093   Reynolds, R. W., N. A. Rayner, T. M. Smith, D. C. Stokes and W. Wang (2002), An improved in situ
1094   and satellite SST analysis for climate. *J. Climate*, 15, 1609-1625.
1095

1096 Richey, J. E., Melack, J. M., Aufdenkampe, A. K., Ballester, V. M. & Hess, L. L. (2002), Outgassing
1097 from Amazonian rivers and wetlands as a large tropical source of atmospheric CO2. Nature 416,
1098 617–620.
1099
1100 Rödenbeck, C., S. Houweling, M. Gloor, and M. Heimann (2003), CO_2 flux history 1982-2001
1101 inferred from atmospheric data using a global inversion of atmospheric transport, *Atmos. Chem.*
1102 *Phys.*, *3*(6), 1919-1964.
1103 Rödenbeck, C., D. C. E. Bakker, N. Metzl, A. Olsen, C. Sabine, N. Cassar, F. Reum, R. F. Keeling,
1104 and M. Heimann, (2014), Interannual sea–air CO2 flux variability from an observation-driven
1105 ocean mixed-layer scheme, Biogeosciences Discuss., 11, 3167– 3207, doi:10.5194/bgd-11-3167-
1106 2014.
1107
1108 Scholze, M., P. Ciais, and M. Heimann (2008), Modeling terrestrial ^{13}C cycling: Climate, land use
1109 and fire, *Global Biogeochem. Cycles*, 22, GB1009, doi:10.1029/2006GB002899.
1110 Siegenthaler, U. and H. Oeschger (1987). Biospheric CO2 emissions during the past 200 years
1111 reconstructed by deconvolution of ice core data. *Tellus* 39B, 140-154.
1112 Sprintsin, M., J. M. Chen, and P. Czurylowicz (2011), Combining land surface temperature and
1113 shortwave infrared reflectance for early detection of mountain pine beetle infestations in western
1114 Canada. *Journal of Applied Remote Sensing* 5(1), 053566.
1115 Steinkamp, K., and N. Gruber (2013), A joint atmosphere-ocean inversion for the estimation of
1116 seasonal carbon sources and sinks, *Global Biogeochem. Cycles*, *27*, doi:10.1002/gbc.20064.
1117
1118 Stephens, B., et al. (2007), Weak northern and strong tropical land carbon uptake from vertical
1119 profiles of atmospheric CO2, *Science*, *316*(5832), 1732–1735.
1120
1121 Suits, N. S., A. S. Denning, J. A. Berry, C. J. Still, J. Kaduk, J. B. Miller, and I. T. Baker (2005),
1122 Simulation of carbon isotope discrimination of the terrestrial biosphere, *Global Biogeochem. Cycles*,
1123 19, GB1017, doi:10.1029/2003GB002141.
1124
1125 Still, C. J., J. A. Berry, G. J. Collatz, and R. S. DeFries (2003), Global distribution of C3 and C4
1126 vegetation: Carbon cycle implications, *Global Biogeochem. Cycles*, 17(1), 1006, doi: 10.1029 / 2001
1127 GB001807.
1128
1129 Tans, P. P., I. Y. Fung, and T. Takahashi (1990), Observational Contrains on the Global Atmospheric
1130 CO_2 Budget, *Science*, *247*(4949), 1431-1438.
1131
1132 Tans, P. P., J. A. Berry, and R. F. Keeling (1993), Oceanic ^{13}C data: A new window on CO_2 uptake
1133 by the oceans, *Global Biogeochem. Cycles*, 7, 353-368.
1134
1135 Tarantola, A. (1987), *Inverse Problem Theory*, 605 pp., Elsevier, Amsterdam, The Netherlands.
1136

van der Velde, I. R., J. B. Miller, K. Schaefer, K. A. Masarie, S. Denning, J. W. C. White, P. P. Tans, M. C. Krol, and W. Peters (2013), Biosphere model simulations of interannual variability in terrestrial 13C/12C exchange, *Global Biogeochemical Cycles,* 27, 637–649

van der Werf, G. R., J. T. Randerson, L. Giglio, G. J. Collatz, P. S. Kasibhatla, and A. F. Arellano Jr. (2006), Interannual variability of global biomass burning emissions from 1997 to 2004, *Atmos. Chem. Phys. Discuss.*, *6*(2), 3175-3226.

Webb, R. S., C. E. Rosenzweig, and E. R. Levine (1991), A global data set of soil particle size properties, *NASA Tech. Memo.*, TM-4286, 40 pp.

Wanninkhof, R., G. -H. Park, T. Takahashi, C. Sweeney, R. Feely, Y. Nojiri, N. Gruber, S. C. Doney, G. A. McKinley, A. Lenton, C. Le Quéré, C. Heinze, J. Schwinger, H. Graven, and S. Khatiwala, (2013), Global ocean carbon uptake: magnitude, variability and trends, Biogeosciences, 10, 1983-2000, doi:10.5194/bg-10-1983-2013,

Zhang F., J. M. Chen, J. Chen, C. M. Gough, T. A. Martin, D. Dragoni (2012), Evaluating spatial and temporal patterns of MODIS GPP over the conterminous U.S. against flux measurements and a process model, *Remote Sensing of Environment*, Vol. 124: 717-729.

Zhang S.P., X. Yi, X. G. Zheng, Z. Q. Chen, et al., 2014. Global Carbon Assimilation System using a Local Ensemble Kalman Filter with Multiple Ecosystem Models, *Journal of Geophysical Research-Biogeosciences*, doi: 10.1002/2014JG002792.

1162 **Table 1.** Biophysical parameters are assigned by plant functional types in BEPS. References for the
1163 chosen values of these parameters are found in *Chen et al*. (2012).

Parameters[*]	Broadleaf Evergreen	Broadleaf Deciduous	Evergreen Conifers	Deciduous Conifers	Shrub	C4 Plants	Others
V_{cmax} μmol m^{-2} s^{-1} (at 25°C)	29.0±7.7	57.7±21.2	62.5±24.7	39.1±11.7	57.9±19.6	100.7±36.6	90.0±89.5
J_{max} μmol m^{-2} s^{-1}	55.1	123.7	135.2	79.2	124.1	193.1	200.0
N g m^{-2}	2.17±0.8	1.74±0.71	3.10±1.35	1.81±0.64	1.86±0.84	1.62±0.61	1.69±0.69
χ_n m^2 g^{-1}	0.48	0.59	0.33	0.56	0.57	0.62	0.60
Slope (m)	8	8	8	8	8	4	8
Intercept (b), mol m^{-2} s^{-1}	0.0011	0.0011	0.0011	0.0011	0.0011	0.0011	0.0011
LAI	4.07±2.02	3.14±1.99	3.05±1.62	2.42±1.45	1.49±1.06	1.55±1.22	1.64±1.15
Clumping Index	0.66±0.045	0.70±0.047	0.74±0.057	0.78±0.051	0.75±0.059	0.75±0.050	0.76±0.059
Canopy height (m)	23	23	20	20	4	4	4

1164 Where V_{cmax} is the leaf maximum carboxylation rate at 25°C, J_{max} is the maximum electron transport rate, N is the leaf nitrogen content, χ_n is the slope
1165 of V_{cmax} variation with N, and m and b are the slope and intercept in the Ball-Berry equation. The peak growing season LAI and clumping index are
1166 given as the mean and standard deviation for each plant functional type.
1167

1168

1169

1170 Table 2. Global average ages of soil carbon pools computed by BEPS with consideration of the
1171 influences of temperature and soil moisture on the decomposition rates of these pools.
1172

1173

Soil carbon pool i	Name	Global Average Age τ_i (yr)
1	Surface structural leaf litter	5.0
2	Surface metabolic leaf litter	2.3
3	Soil structural litter	4.4
4	Soil metabolic litter	2.3
5	Woody litter	34.9
6	Surface microbe	11.1
7	Soil microbe	28.5
8	Slow carbon	35.5
9	Passive carbon	667.9

1174
1175

1176 Table 3. Inverted fluxes (Pg C y^{-1}), averaged for 2002 –2004, for land and ocean regions with (CO_2 +
1177 $^{13}CO_2$) and without (CO_2 only) ^{13}C constraint. The negative sign denotes the flux from the
1178 atmosphere to the surface (sink). Various treatments are made to ^{13}C discrimination and
1179 disequilibrium fluxes represented by the following cases:

1180 Case I: Full consideration of the regional differences in discrimination and disequilibrium;

1181 Case II: Same as Case I, but the annual photosynthetic discrimination ratio is set at a constant of -
1182 14.1‰, although it's monthly variation pattern as modeled by BEPS is retained;

1183 Case III: Same as Case I, but the disequilibrium flux over land is ignored;

1184 Case IV: Same as Case I, but the disequilibrium flux over ocean is ignored;

1185 Case V: Same as Case I, but the disequilibrium flux over both land and ocean is ignored.

1186

1187

Region	Prior flux	Double De-convolution	Inverted CO_2 flux						
			CO_2 data	CO_2 + $^{13}CO_2$ data					
				Case I	Case II	Case III	Case IV	Case V
Land	-2.61 ±2.07	-2.90	-3.40 ±0.84	-2.53 ±0.93	-2.49 ±0.95	-3.58 ±0.93	-2.66 ±0.93	-3.71 ±0.93
Ocean	-2.13 ±0.67	-2.36	-1.48 ±0.40	-2.36 ±0.49	-2.35 ±0.48	-2.24 ±0.49	-4.44 ±0.49	-4.32 ±0.49

1188

1189

1190

1191   Table 4. Comparison of land and ocean disequilibrium coefficients and disequilibrium fluxes
1192   calculated in this study with those in previous studies.

1193

1194

Studies	Year	Land Disequilibrium Coefficient (‰)	Land Disequilibrium Flux (PgC y^{-1} ‰)	Ocean Disequilibrium Coefficient (‰)	Ocean Disequilibrium Flux (PgC y^{-1} ‰)
This study	2002-2004	0.49	26.8	0.78	66
Fung et al. (1997)	1988	0.33	N/A	N/A	N/A
Randerson et al. (2002)	1981-1994	0.33	20	0.6	55
Alden et al. (2010)	1991-2007	0.45-0.61	22.7-30.6	N/A	92.3-100.2 (globe total)
Van der Velde et al. (2013)	1991-2007	0.486	25.4	N/A	48.7
Francey et al. (1995)	1987	0.43	25.8	0.48	43.8

1195 Table 5. Global isotopic mass budgets averaged for the 2002-2004 period for the prior, double de-
1196 convolution, CO_2-only inversion, and joint inversion (unit: Pg C y^{-1} ‰). Also shown are ocean and
1197 land net fluxes (unit Pg C y^{-1}) for these cases for comparison purposes. For the prior fluxes, the
1198 component of each flux are indicated in the brackets. The isotopic coefficients are same among the
1199 cases.

Isotopic terms	Prior	Double de-convolution	CO_2 –only inversion	Joint inversion
$-C_a\, d(\delta_a)/dt$	15.0 [750 Pg C×(-0.02‰ y^{-1})]	15.0	15.0	15.0
$F_f\,(\delta_f - \delta_a)^*$	-153.7 [8.9 Pg C y^{-1}×(-17.27‰)]	-153.7	-153.7	-153.7
$-(F_{lph} - F_{lb})\varepsilon_{lh}$	36.7 [2.6 Pg C y^{-1}×(-14.10‰)]	40.9	47.9	39.5
$F_{lb}(\delta_{lb} - \delta_{lbe})$	26.8 [54.7 Pg C y^{-1}×(-0.49‰)]	26.8	26.8	26.8
$-(F_{ao} - F_{oa})\varepsilon_{ao}$	4.2 [2.1 Pg C y^{-1}×(-2.00‰)]	4.8	3.0	4.6
$F_{oa}\,(\delta^e_{oa} - \delta_{oa})$	66.0 [84.6 Pg C y^{-1}×(-0.78‰)]	66.0	66.0	66.0
Global Budget	-5.0	0.8	-5.0	1.8
$(F_{lph} - F_{lb})$, Pg C y^{-1}	-2.6	-2.9	-3.4	-2.8
$(F_{ao} - F_{oa})$, Pg C y^{-1}	-2.1	-2.4	-1.5	-2.3

1200 *F_f is the carbon emission from fossil fuel and biomass burning, 6.9 and 2.1, Pg C y^{-1}, respectively,
1201 and δ_f is weighted average 13C composition for fossil fuel and biomass burning, being 25.27‰, and δ_a=-8.0‰.

1202

1203

1204 Table 6. Inverted fluxes (Pg C y^{-1}), averaged for 2002 –2004, for land and ocean regions using ^{13}C

1205 data only. The negative sign denotes the flux from the atmosphere to the surface (sink). Various

1206 treatments are made to ^{13}C discrimination and disequilibrium fluxes represented by the cases outlined

1207 in Table 3.

1208

Region	Prior flux	Inverted CO$_2$ flux				
		^{13}CO$_2$ data				
		Case I	Case II	Case III	Case IV	Case V
Land	-2.61 ±2.07	-2.60 ±0.96	-2.56 ±0.99	-3.61 ±0.96	-2.65 ±0.96	-3.66 ±0.96
Ocean	-2.13 ±0.67	-2.28 ±0.53	-2.27 ±0.54	-2.28 ±0.53	-4.65 ±0.53	-4.65 ±0.53

1209

1210

1211

1212

1213   **Figures**

1214

1215   Figure 1. A global nested inversion system with a focus in North America, in which oceans are

1216   divided into 11 regions and land areas are divided into 9 large and 30 small regions outside and

1217   within North America, respectively. Also shown are CO_2 and $^{13}CO_2$ observation stations included in

1218   the GlobalView database and used in this study. 10 of the stations are marked with their names

1219   because they are selected to compare prior and posterior concentrations in Figure 11.

1220

1221

1222

1223

1224
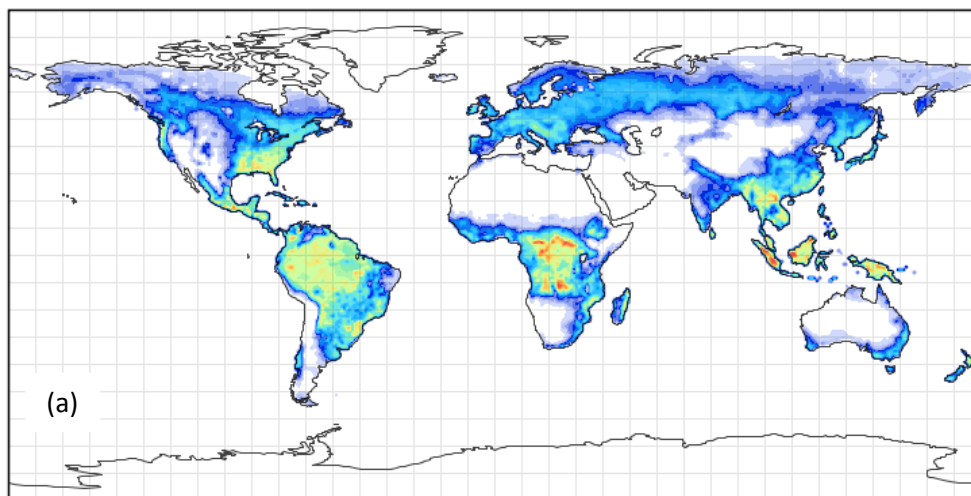
1225
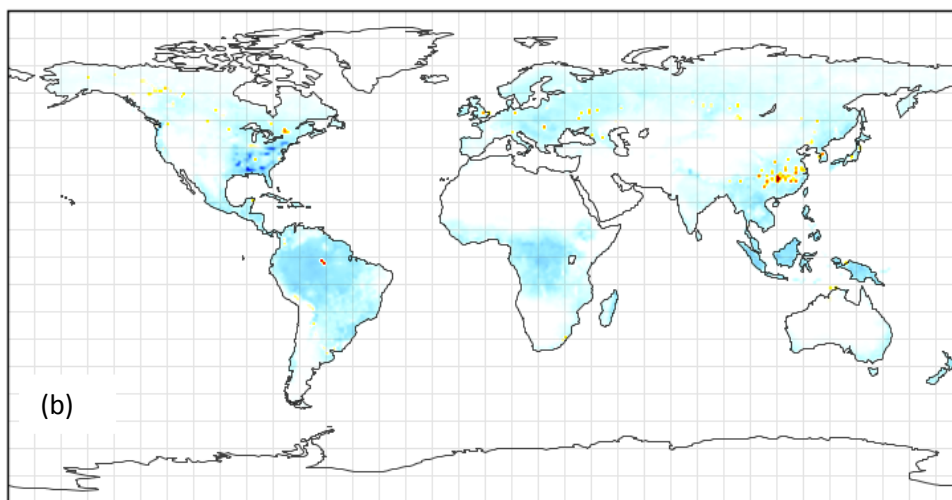
1226

Figure 2. (a) gross primary productivity (GPP) distribution in 2003 computed using remote sensing LAI and land cover maps and climate and soil data, and (b) net ecosystem productivity (NEP) distribution in 2003. Both are calculated using the BEPS model. Annual NEP maps from 2000 to 2004 are used to as the prior flux in the inversions. This GPP map is used to distribute the flux uncertainty among the 39 land regions.
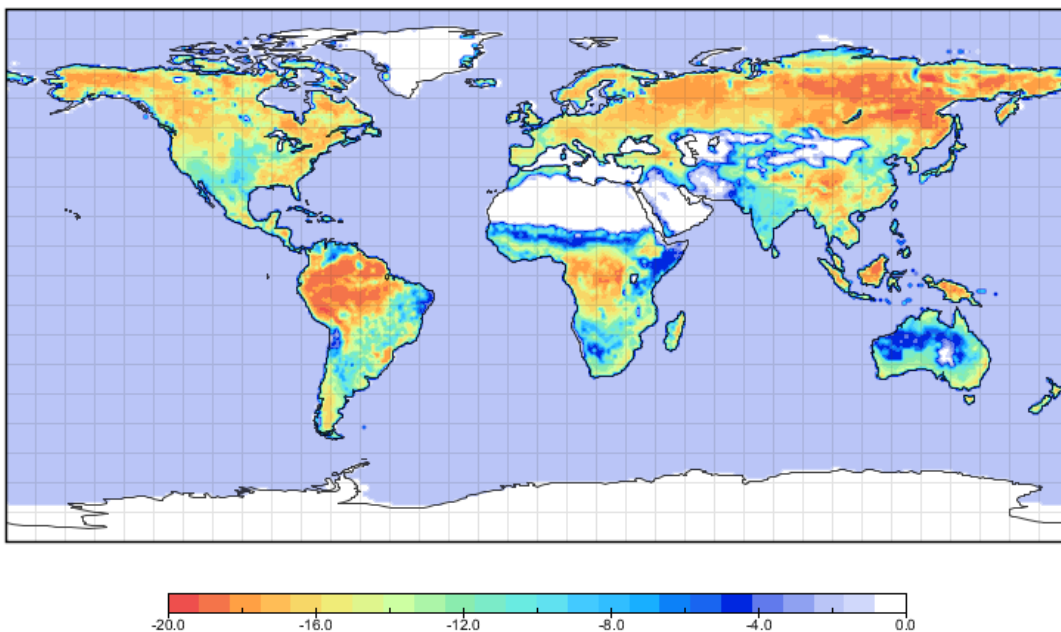
1232

1233   Figure 3. The annual mean of the total photosynthetic ^{13}C discrimination ($\varDelta$ in Eq. 7) in 2003.

1234
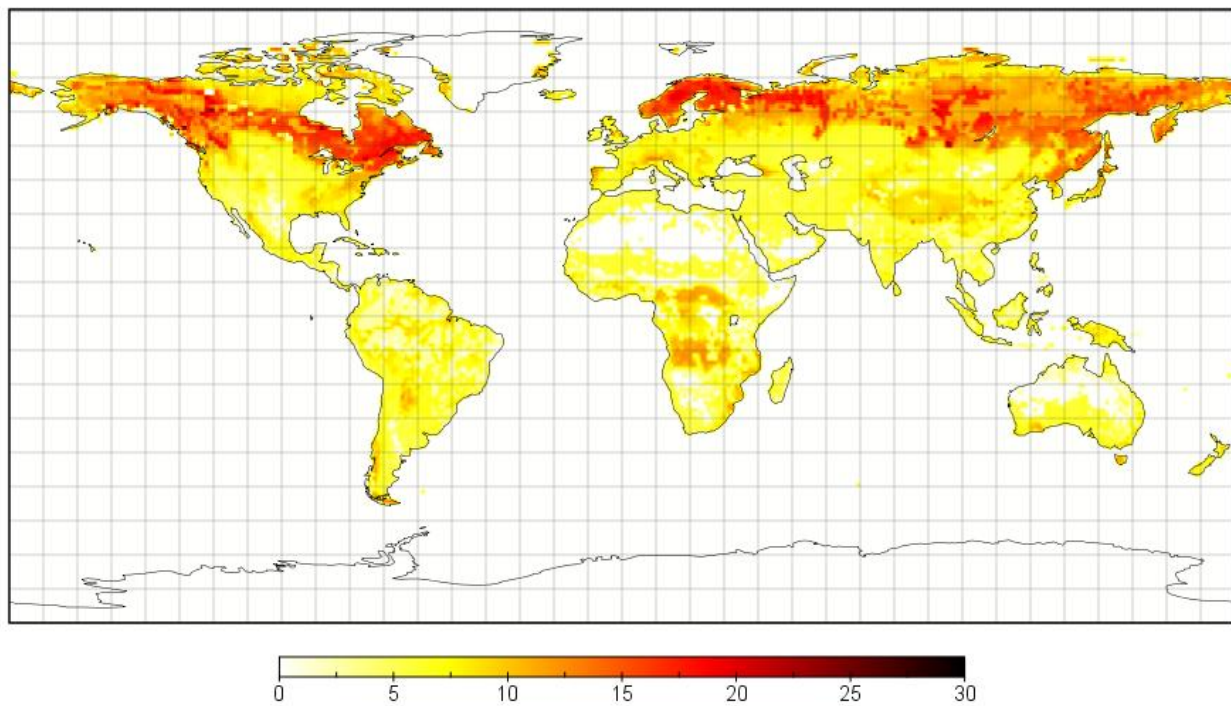
1235

1236   Figure 4. Global distribution of the flux-weighted mean age of soil carbon pools (Eq. 8).

1237

1238

1239

1240
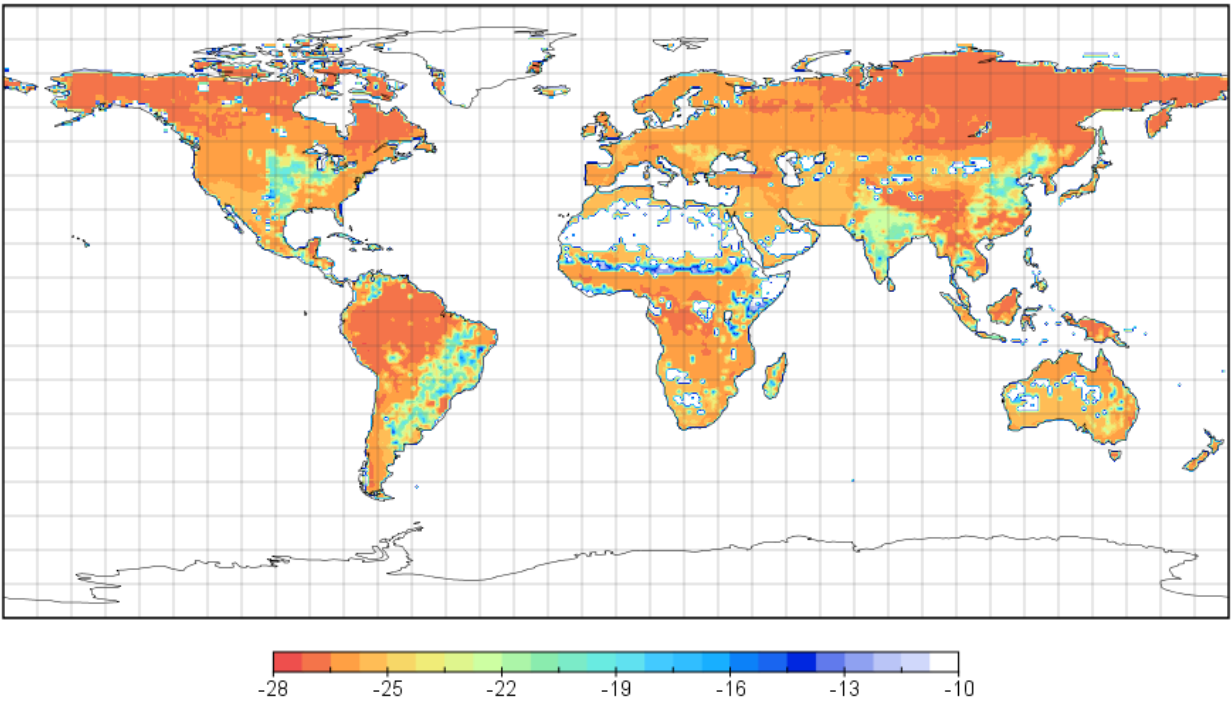
1241

1242 Figure 5. Global δ^{13}C distribution over land (annual flux-weighted average in 2003).

1243
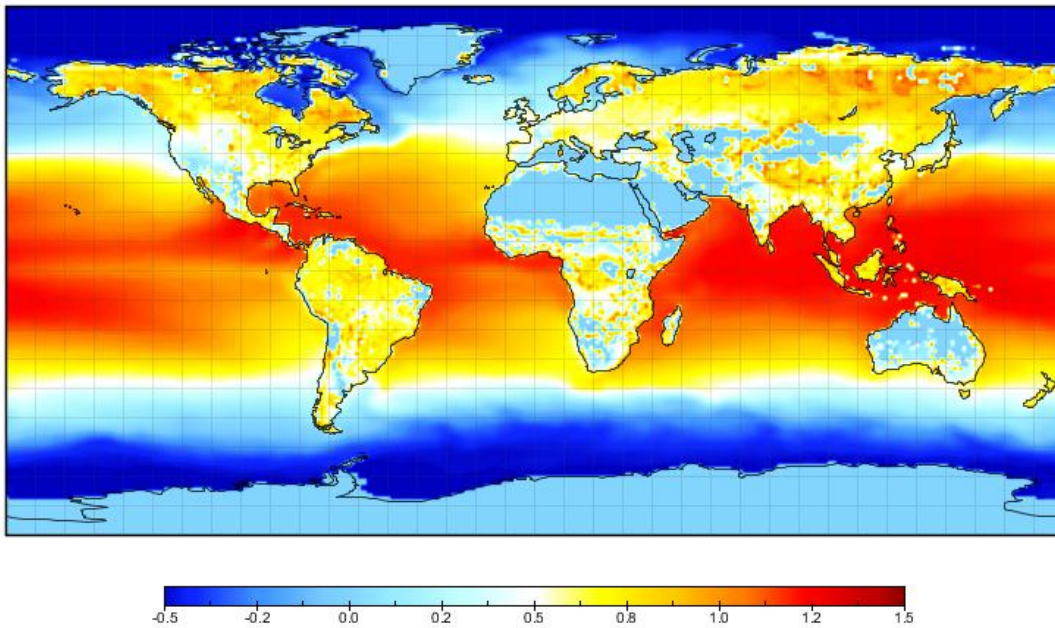
1244

1245

1246   Figure 6. Disequilibria between ^{13}C fluxes to and from the land or ocean surface in 2000. At the land

1247   surface, the disequilibrium is the difference between photosynthetic and respiratory discriminations

1248   against ^{13}C, and at the ocean surface, it is the difference in ^{13}C discrimination between the one-way

1249   diffusive downward and upward fluxes.

1250

1251
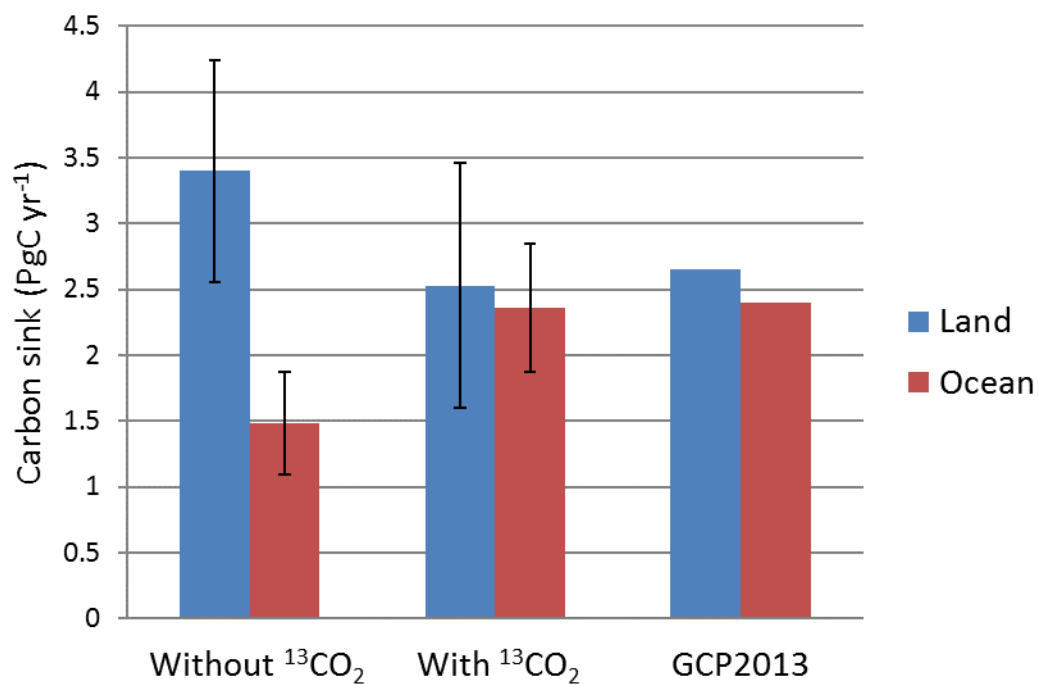
1252   Figure 7. Comparison of land and ocean carbon sinks derived from inversions with and without the

1253 $^{13}CO_2$ constraint against the Global Carbon Project results (*Le Quéré et al.*, 2013).

1254

1255
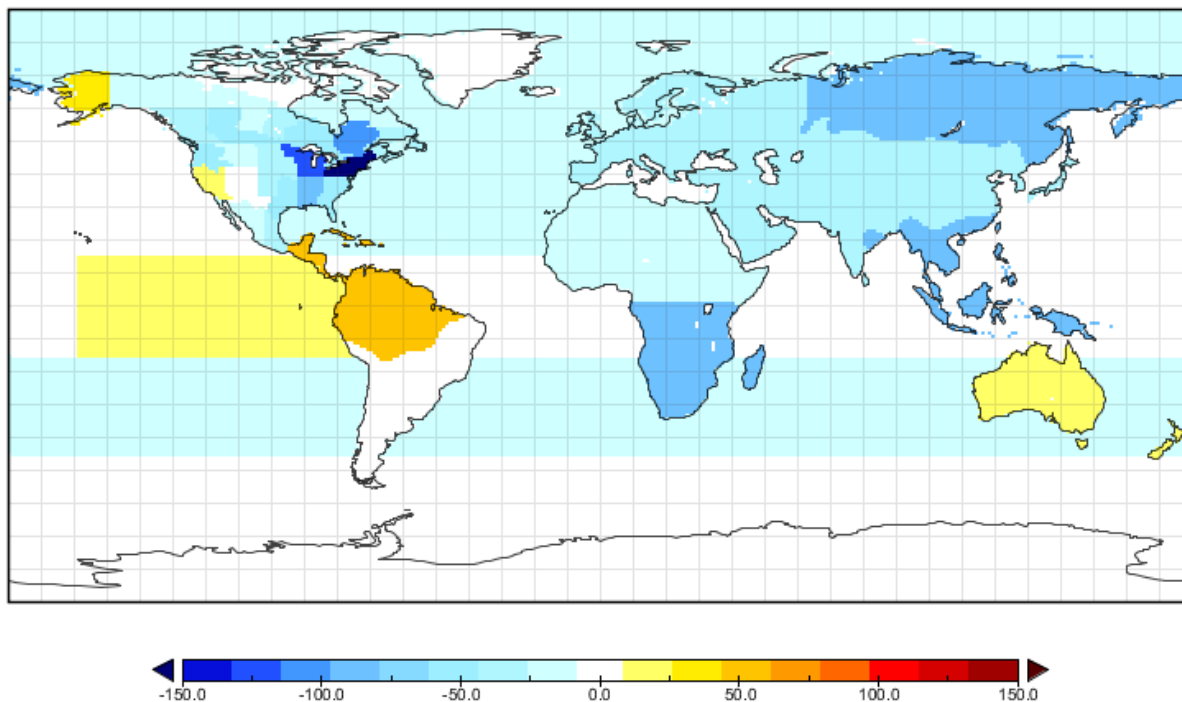
1256

1257   Figure 8. Global distribution of inverted CO_2 flux using CO_2 data only ($(gC\ m^{-2}y^{-1}$, 2002-2004

1258   average).

1259

1260

1261

1262
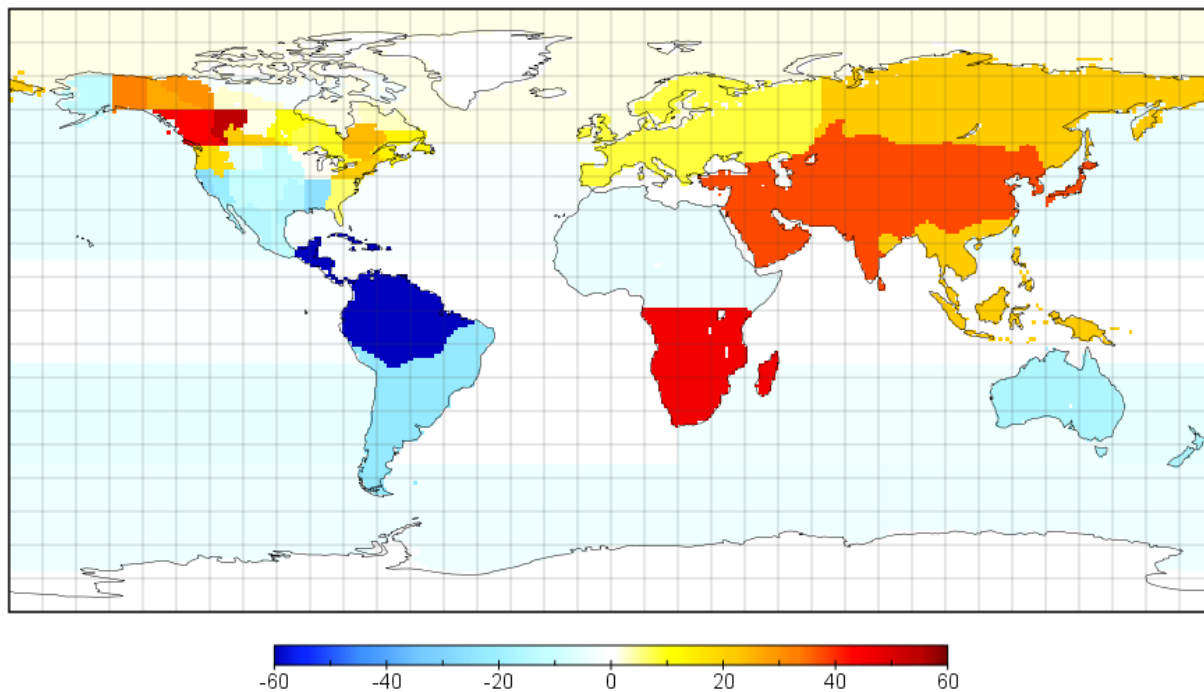
1263

1264   Figure 9. Difference of the inverted CO_2 flux between using $CO_2 + {}^{13}CO_2$ data and using CO_2 data

1265   only (gC m^{-2}y^{-1}, 2002-2004 average).

1266

1267

1268

1269

1270

1271

1272

1273

1274
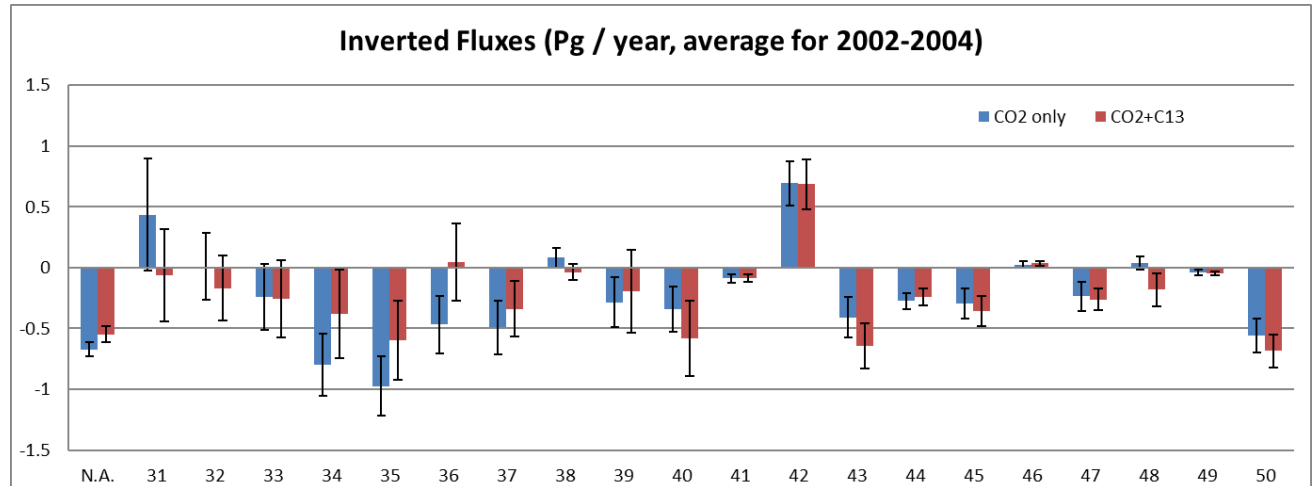
1275

1276   Figure 10. Comparison between inversion results with and without $^{13}CO_2$ constraint for 21 regions of

1277   the globe for the periods of 2002-2004.

1278

1279

1280
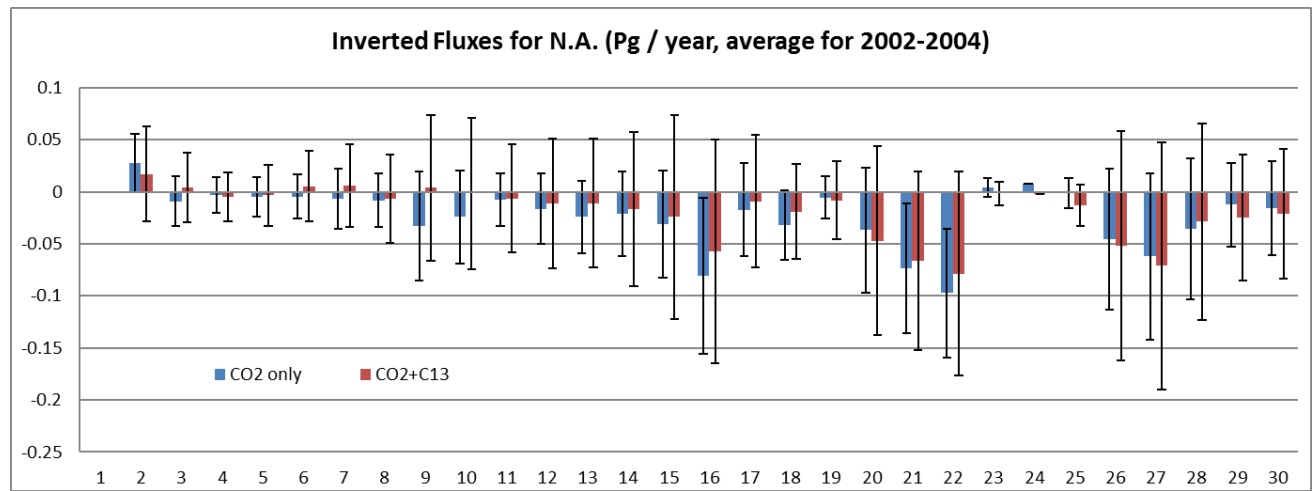
1281

1282 Figure 11. Comparison between inversion results with and without $^{13}CO_2$ constraint for 30 regions in

1283 North America.

1284

1285
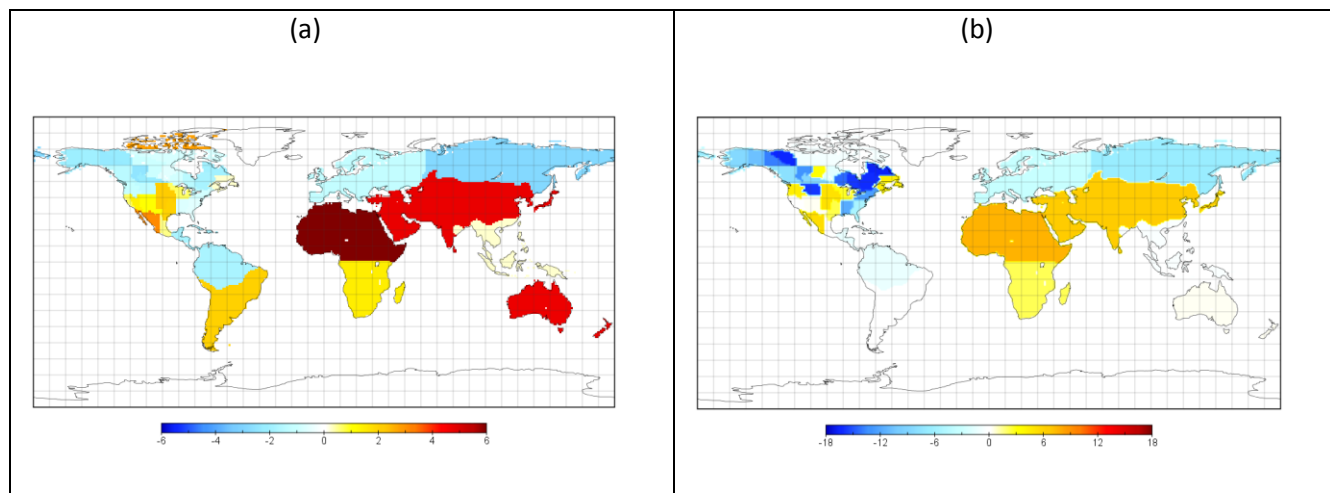
Figure 12. (a) Difference in ε_{lph} (‰) and (b) the inverted CO_2 flux (gC m^{-2}y^{-1}) between Case I and Case II, i.e. Case I minus Case II. See Section 2.1.3 for the description of these cases.

1291
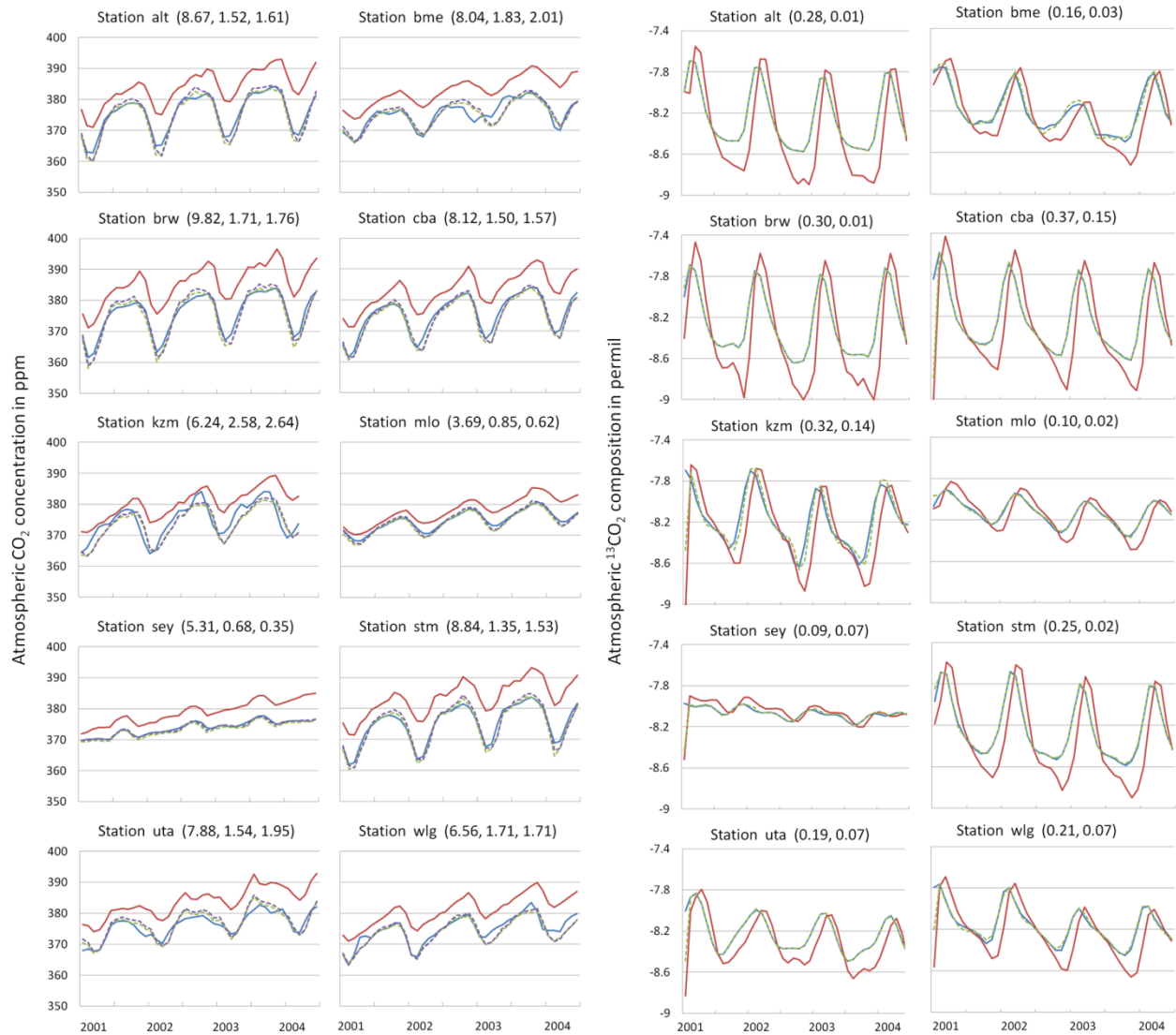
1292

Figure 13. Left panel: comparison of CO_2 concentrations calculated using the prior flux (solid red)
and from CO_2-only inversion (dashed purple) and joint inversion (dashed green) against observations
(green) at 10 randomly selected stations from different regions. The header of each plot indicates the
station ID and the root mean square difference (RMSD) for the prior, joint and CO_2-only inversions
against observations. Right panel: comparison of $^{13}CO_2$ composition from the prior (solid red) and
joint inversion (dashed purple) against observations (green). The header of each plot indicates the
station ID and RMSD of the prior and the joint inversion against observations.

1300

1301
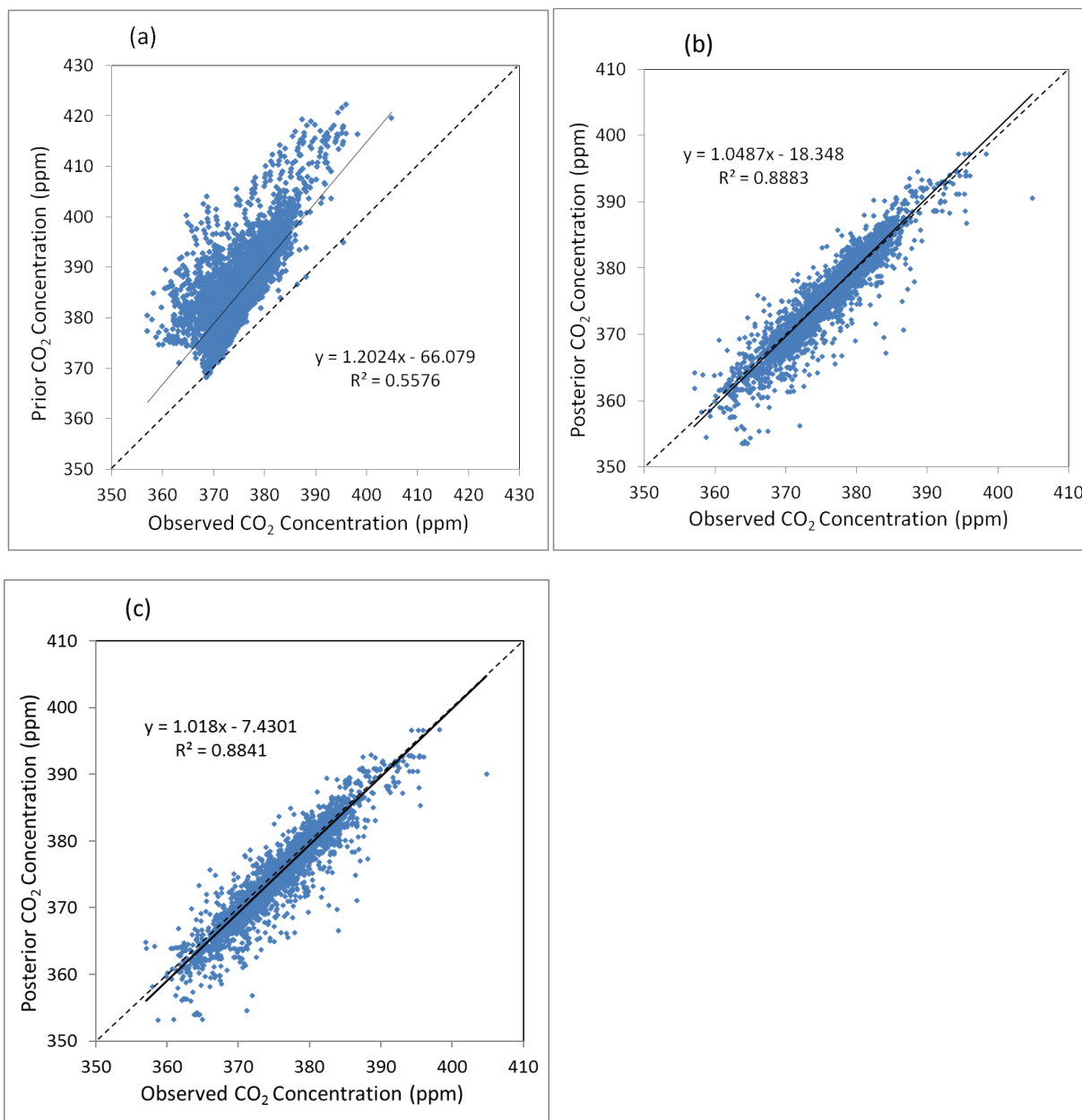
Figure 14. CO_2 concentrations from (a) prior, (b) posterior from the CO_2-only inversion, and (c) posterior from the joint inversion in comparison with observations. The prior concentration is obtained through transport modeling with prior CO_2 fluxes from the terrestrial ecosystems, oceans, fossil fuel emission, and biomass burning.

1312

1313

1314
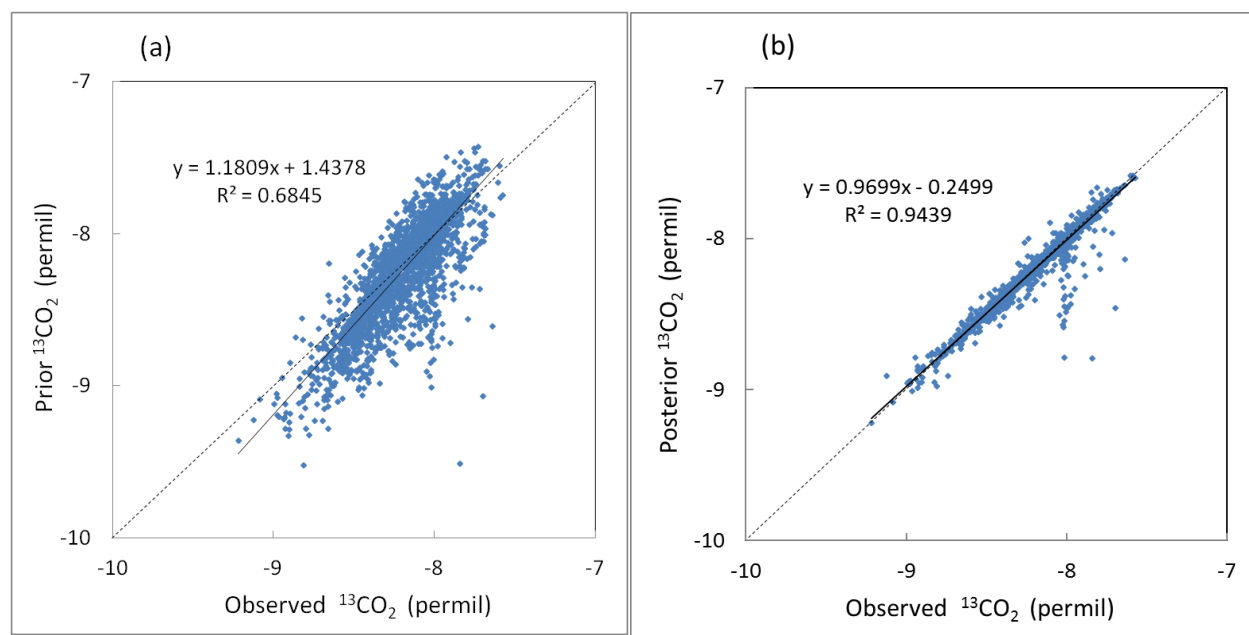
1315 Figure 15. Comparison of prior (a) and posterior (b) $^{13}CO_2$ compositions with observations. The prior
1316 composition is obtained through transport modeling with prior $^{13}CO_2$ fluxes from the terrestrial
1317 ecosystems, oceans, fossil fuel emission, and biomass burning, and the posterior composition is
1318 obtained with the CO_2-$^{13}CO_2$ joint inversion (Case I).

1319

1320

1321

1322

1323

1324